Nonlinear incremental control for flexible aircraft trajectory tracking and load alleviation

Wang, Xuerui; Mkhoyan, Tigran; De Breuker, Roeland

DOI
10.2514/1.G005921

Publication date
2022

Document Version
Final published version

Published in
Journal of Guidance, Control, and Dynamics

JOURNAL OF GUIDANCE, CONTROL, AND DYNAMICS
Vol. 45, No. 1, January 2022

Nonlinear Incremental Control for Flexible Aircraft Trajectory Tracking and Load Alleviation

Xuerui Wang,* Tigran Mkhoyan,† and Roeland De Breuker‡
Delft University of Technology, 2629 HS Delft, The Netherlands

https://doi.org/10.2514/1.G005921

This paper proposes a nonlinear control architecture for flexible aircraft simultaneous trajectory tracking and load alleviation. By exploiting the control redundancy, the gust and maneuver loads are alleviated without degrading the rigid-body command tracking performance. The proposed control architecture contains four cascaded loops: position control, flight path control, attitude control, and optimal multi-objective wing control. Because the position kinematics are not influenced by model uncertainties, the nonlinear dynamic inversion control is applied. On the contrary, the flight path dynamics are perturbed by both model uncertainties and atmospheric disturbances; thus the incremental sliding mode control is adopted. Lyapunov-based analyses show that this method can simultaneously reduce the model dependency and the minimum possible gains of conventional sliding mode control methods. Moreover, the attitude dynamics are in the strict-feedback form; thus the incremental backstepping sliding mode control is implemented. Furthermore, a novel load reference generator is designed to distinguish the necessary loads for performing maneuvers from the excessive loads. The load references are realized by the inner-loop optimal wing controller, whereas the excessive loads are naturalized by flaps without influencing the outer-loop tracking performance. The merits of the proposed control architecture are verified by trajectory tracking tasks in spatial von Kármán turbulence fields.

I. Introduction

THE pursuit of higher efficiency has driven aircraft design evolving toward having higher aspect ratios and more lightweight structures. The resulting increase in structural flexibility makes the conventional frequency separation between rigid-body and structural degrees of freedom unreliable [1,2]. During aggressive flight maneuvers or in the presence of gusts, structural integrity is also challenged. Given this background, there has been increasing interest in flexible aircraft control algorithms that can achieve multiple objectives, which include traditional pilot command-following flight control, gust load alleviation (GLA), maneuver load alleviation (MLA), flutter suppression [3], drag minimization, etc.

In the literature, it is a common practice to design two independent controllers, one for rigid-body command tracking and another for fulfilling the remaining objectives (GLA, MLA, flutter suppression, etc.) [3–6]. As reported in [4], conflict can occur if the roll tracking command and the load alleviation command are given to the same wing trailing-edge control surface. To avoid this conflict, the aerodynamic control surfaces are usually classified into two sets. For example, in [4], two inboard elevators are used for pitch control, two outboard elevators are used for roll control, whereas all the ailerons are used for GLA. A model prediction controller is designed for MLA in [6]; the outboard ailerons are used to achieve MLA, whereas the inboard ailerons, together with elevator and rudder, are selected for rigid-body control. In the real-world flight tests of a flexible UAV, the outboard flaps are selected for flutter suppression (a gain-scheduled H_∞ control), whereas the midboard flaps and ruddervators are reserved for a baseline rigid-body controller [3]. A similar selection is also adopted in [5] for executing the commands provided by linear-quadratic regulators. However, the selection and isolation cannot make full use of the control input space and can cause a large gap between two adjacent flaps. An integrated controller that considers both rigid-body and aeroelastic control objectives, while using the control redundancy, is desirable.

Another challenge faced by multi-objective flexible aircraft flight control algorithms is the balance between load alleviation performance and rigid-body command tracking performance [7]. For example, the simulation results in [8] show that the pitch rate command tracking is poor because the MLA function is designed to reduce the wing root bending moment [8]. Essentially, if a flexible aircraft has more than three independent control surfaces, and if not all of them are in the aircraft symmetrical plane, then there are infinite deflection combinations to realize the conventional three-axis attitude control moments. In other words, such an aircraft is overactuated in rigid-body command tracking tasks. Therefore, it is physically realistic to simultaneously achieve desired rigid-body control moments together with other objectives (such as load alleviation), rather than making tradeoffs among them.

Recently, a control method that can alleviate loads without changing rigid-body tracking performance is presented in [9,10]. By exploiting the null space between the input and rigid-body output, the load alleviation objective is decoupled from the rigid-body tracking objective. However, this method has two main limitations: first, the design of the null space filters strongly depends on the matrix fraction description of the linear state-space model, and thus the decoupling effectiveness is questioned in the presence of model uncertainties and unmodeled nonlinearities; second, the proposed controller only ensures that the load bounds are not violated, but does not further minimize the load variations within the bounds. These two issues will be tackled using incremental control in this paper.

Incremental control refers to a class of nonlinear control methods that replace a part of model information by sensor measurements. The most well-known incremental control method is the incremental nonlinear dynamic inversion (INDI) control, which reduces the model dependency and enhances the robustness of the well-known nonlinear dynamic inversion (NDI) control [11,12]. These properties have stimulated the application of INDI to various aerospace systems (a CS-25 certified aircraft [13], quadrotors [14], launch vehicles [15], etc.). Recently, Ref. [16] presented more generalized derivations, as well as Lyapunov-based stability and robustness analyses for the

Presented as Paper 2021-0503 at the AIAA Scitech 2021 Forum, Virtual Event, 11–15 & 19–21, January 2021; received 13 January 2021; revision received 25 June 2021; accepted for publication 29 June 2021; published online 26 August 2021.

*Assistant Professor, Department of Aerospace Structures and Materials, and Department of Control and Operations, Faculty of Aerospace Engineering; x.wang-6@tudelft.nl. Member AIAA.

†Ph.D. Candidate, Department of Aerospace Structures and Materials, Faculty of Aerospace Engineering, Kluyverweg 1; t.mkhoyan@tudelft.nl. Student Member AIAA.

‡Associate Professor, Department of Aerospace Structures and Materials, Faculty of Aerospace Engineering, Kluyverweg 1; r.debreuker@tudelft.nl. Senior Member AIAA.

INDI control. Theoretical analyses also show that INDI is more robust than the NDI control used in [17]. The INDI control law has been used to solve a free-flying flexible aircraft GLA problem in [18]. The control objectives of rigid-body motion regulation, GLA, and structural vibration suppression are achieved simultaneously. Moreover, theoretical analyses and various time-domain simulations demonstrate the robustness of INDI control to atmospheric disturbance, aerodynamic model uncertainties, and even actuator faults. Apart from these merits, the controller designed in [18] also has limitations. Because the number of controlled states is higher than the number of control inputs, the weight-least square method is used in the INDI loop for making tradeoffs among different virtual control channels. As a consequence, not all the designed virtual controls can be fully executed. Although this control structure works well for the GLA problem, it would degrade aircraft tracking performance if is directly extended to MLA problems. In view of these issues, a different control architecture will be proposed in this paper.

To further expand the applicability and enhance the robustness of INDI control, the incremental sliding mode control framework (INDI-SMC) was proposed in [19]. In the literature, the majority of (high-order) sliding mode achievements depend on a model-based control structure [20–22]. However, this common practice is facing a dilemma: on the one hand, pursuing decent models is challenging and costly for complex dynamic systems; on the other hand, a reduced model accuracy would demand amplified sliding mode control and observer gains for resisting uncertainties, which can lead to amplifications of noise and chattering. This dilemma can be solved by the sensor-based control structure of INDI-SMC, where minimum possible control/observer gains as well as the model dependency can be simultaneously reduced. Theoretical proofs and simulations demonstrate that a wide range of model uncertainties, sudden actuator faults, and structural damage can be passively resisted by INDI-SMC, without using additional fault detection and isolation modules [19]. The hybridization idea was carried forward in [23], where the incremental backstepping sliding mode control (IBSMC) is proposed for multi-input/multi-output nonlinear strict-feedback perturbed systems. Theoretical analyses and simulations show that IBSMC not only has less model dependency but also has enhanced robustness than model-based backstepping sliding mode control in the literature. These advantages make INDI-SMC and IBSMC promising for solving flexible aircraft control problems.

The main contribution of this paper is a nonlinear control architecture designed for flexible aircraft trajectory tracking and load alleviation purposes. The proposed control architecture has the following features: 1) it has enhanced robustness against model uncertainties, external disturbances, and faults despite its reduced model dependency; 2) it contains a load reference generator to distinguish the loads that are necessary to perform maneuvers from the excessive loads; 3) it can neutralize the excessive loads without degrading the rigid-body tracking performance, no matter the excessive loads are induced by maneuvers or atmospheric disturbances.

Apart from the control design, the kinematics and dynamics of a free-flying flexible aircraft are also derived in this paper. A body-fixed reference frame is used to capture both the inertial and aerodynamic couplings between the rigid-body and structural degrees of freedom. Furthermore, a modular approach to conveniently make an existing clamped-wing aeroservoelastic model free-flying is presented in this paper. This modular approach contributes to bridging the flight dynamics and aeroelasticity communities.

The rest of this paper is structured as follows. The flexible aircraft kinematics and dynamics are derived in Sec. II. The nonlinear control architecture is presented in Sec. III. The simulation results are presented in Sec. IV with the conclusions drawn in Sec. V. Supplements to the dynamic equations are given in the Appendix. In this paper, bold symbols represent vectors and matrices.

II. Model Descriptions

An overview of the flexible aircraft model used in this paper is shown in Fig. 1.

A. Aeroservoelastic Model of the Wing

In this subsection, the aeroservoelastic model of the wing will be derived in the local wing-fixed reference frame: $\mathcal{F}_W\,(O_w, x_w, y_w, z_w)$ (Fig. 1). The left and right wings are modeled as two beams. The origin O_w is defined at the root of each beam. The axis $O_w x_w$ is aligned with the *undeformed* beam, and $O_w y_w$ is aligned with the mean chord. The right wing dynamics will be derived as an example, whereas the dynamics of the left wing can be derived analogously. The rigid-body motions influence the wing dynamics in two aspects: 1) change the local angle of attack; 2) cause additional inertial forces if rigid-body translational and rotational accelerations are nonzero. Both the aerodynamic and inertial influences of rigid-body motions will be considered in the derivations.

1. Structural Model

The dynamic modelings for the left and right wings follow the same procedure. Both wings are under the small elastic deformation assumption, which excludes the effects of geometrical nonlinearities. Taking the right wing as an example, it is modeled as a dynamic Euler Bernoulli beam, which is discretized into n_s elements with $n_s + 1$ nodes. At each node, there are three degrees of freedom: transverse displacement w_s (downward positive), torsion θ_s (nose-up positive), and out-of plane bending ϕ_s (bend-up positive). At each node, a flap with a deflection angle β_s is connected to the beam through a rotational spring considering inertial couplings. Define the state vector for this beam-flap system as $\boldsymbol{X}_s = [\boldsymbol{x}_{s,0}^{\intercal}, \ldots, \boldsymbol{x}_{s,n_s}^{\intercal}]^{\intercal} \in \mathbb{R}^{4(n_s+1)}$, where $\boldsymbol{x}_{s,i} = [w_{s_i}, \phi_{s_i}, \theta_{s_i}, \beta_{s_i}]^{\intercal}, i = 0, \ldots, n_s$. Assume that the beam is clamped at the first node, and denote $\boldsymbol{x}_s = [\boldsymbol{x}_{s,1}^{\intercal}, \ldots, \boldsymbol{x}_{s,n_s}^{\intercal}]^{\intercal} \in \mathbb{R}^{4n_s}$, then the corresponding dynamics are

$$\boldsymbol{M}_s\ddot{\boldsymbol{X}}_s + \boldsymbol{K}_s\boldsymbol{X}_s = \begin{bmatrix} \boldsymbol{M}_{s,0} & \boldsymbol{M}_{s,1} \\ \boldsymbol{M}_{s,1}^{\intercal} & \boldsymbol{M}_{s,n_s} \end{bmatrix}\begin{bmatrix} \ddot{\boldsymbol{x}}_{s,0} \\ \ddot{\boldsymbol{x}}_s \end{bmatrix} + \begin{bmatrix} \boldsymbol{K}_{s,0} & \boldsymbol{K}_{s,1} \\ \boldsymbol{K}_{s,1}^{\intercal} & \boldsymbol{K}_{s,n_s} \end{bmatrix}\begin{bmatrix} \boldsymbol{x}_{s,0} \\ \boldsymbol{x}_s \end{bmatrix} = \begin{bmatrix} \boldsymbol{F}_{\text{root}} \\ \boldsymbol{F}_{\text{ext}} \end{bmatrix} \tag{1}$$

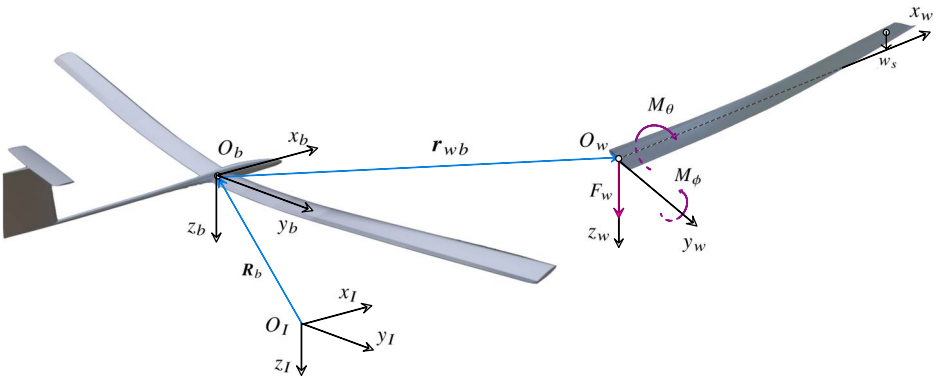

Fig. 1 Reference frames and axis definitions of the flexible aircraft.

where $\boldsymbol{M}_s$ and $\boldsymbol{K}_s$, respectively, represent the structural mass and stiffness matrices. The reaction force at the clamped wing root is denoted as $\boldsymbol{F}_{\text{root}}$. The distributed external force vector is denoted as $\boldsymbol{F}_{\text{ext}}$, which equals the summation of the inertial force $\boldsymbol{F}_{s,\text{acc}}$, the aerodynamic force $\boldsymbol{F}_{s,\text{aero}}$, the gravitational force $\boldsymbol{F}_{s,\text{grav}}$, and the actuation force $\boldsymbol{F}_{s,\text{act}}$.

When the aircraft has translational and rotational accelerations, $\mathcal{F}_W$ becomes a noninertial frame. Therefore, when modeling the structural dynamics in $\mathcal{F}_W$, the inertial couplings induced by rigid-body motions should be considered. These effects are not modeled in the conventional mean-axes method [24]. Consider an infinitesimal mass element d m on an arbitrary section A_w of the wing. When the wing is undeformed, the distance vector from O_w to dm, expressed in $\mathcal{F}_W$, is $\boldsymbol{r}_w = [r_x, r_y, r_z]^\intercal$. The distributed inertial force and moment induced by rigid-body motion per unit length are $\boldsymbol{f}_{\text{acc}} = -\iint_{A_w} \rho \boldsymbol{a}_I \, \mathrm{d}r_y \, \mathrm{d}r_z$ and $\boldsymbol{m}_{\text{acc}} = -\iint_{A_w} \rho [0, r_y, r_z]^\intercal \times \boldsymbol{a}_I \, \mathrm{d}r_y \, \mathrm{d}r_z$, where ρ is the volume density and $\boldsymbol{a}_I$ is derived in Appendix A. These distributed inertial force and moment are integrated to their nearest structural node, leading to $\boldsymbol{F}_{\text{s,acc}} = [[f_w, f_\phi, f_\theta, f_\beta]_{\text{acc},1}, \ldots, [f_w, f_\phi, f_\theta, f_\beta]_{\text{acc},n_s}]^\intercal \in \mathbb{R}^{4n_s}$. The integration process is also presented in Appendix A.

The unsteady strip theory is used to calculate the aerodynamic force $\boldsymbol{F}_{s,\text{aero}}$, which is caused by motions, flap deflections, and external atmospheric disturbances. Discretize the wing into n_a undeformable strips, where each one of them has three degrees of freedom: heave w_a (downward positive), pitching around the elastic axis θ_a (nose-up positive), and flap deflection β_a (downward positive). It is noteworthy that there is no aerodynamic force directly associated with the structural out-of-plane bending degrees of freedom ϕ_s. Based on the indicial function approximation, four lag states per strip are introduced for modeling the circulatory aerodynamics. $[[0, 0, 0, u_1], \ldots, [0, 0, 0, u_{n_s}]]^\intercal = \boldsymbol{H}_u \boldsymbol{u}_w$, where $\boldsymbol{H}_u \in \mathbb{R}^{4n_s \times n_s}$ is a Boolean selection matrix.

2. Wing Aeroservoelastic Dynamic Equations

Typically, the number of aerodynamic strips n_a is larger than the number of structural elements n_s. Therefore, interpolations are required. Two interpolation matrices $\boldsymbol{H}_{as} \in \mathbb{R}^{3n_a \times 4n_s}$ and $\boldsymbol{H}_{sa} \in \mathbb{R}^{4n_s \times 3n_a}$ are needed to couple the structural and aerodynamic degrees of freedom, i.e., $\boldsymbol{x}_a = \boldsymbol{H}_{as}\boldsymbol{x}_s$ and $\boldsymbol{F}_{s,\text{aero}} = \boldsymbol{H}_{sa}\boldsymbol{f}_{\text{aero}}$. Because the origin of the wing-fixed reference frame $\mathcal{F}_W$ coincides with the first structural node, when observing the wing motions in $\mathcal{F}_W$, $\ddot{\boldsymbol{x}}_{s,0} = \dot{\boldsymbol{x}}_{s,0} = \boldsymbol{x}_{s,0} = 0$. Substituting Eq. (2) into Eq. (1), the following state-space system can be derived:

$$\begin{bmatrix} \ddot{\boldsymbol{x}}_s \\ \dot{\boldsymbol{x}}_s \\ \dot{\boldsymbol{z}}_a \end{bmatrix} = \begin{bmatrix} \boldsymbol{M}_{ae}^{-1}\boldsymbol{H}_{sa}\boldsymbol{C}_a\boldsymbol{H}_{as} & \boldsymbol{M}_{ae}^{-1}(\boldsymbol{H}_{sa}\boldsymbol{K}_a\boldsymbol{H}_{as} - \boldsymbol{K}_{s,n_s}) & \boldsymbol{M}_{ae}^{-1}\boldsymbol{H}_{sa}\boldsymbol{K}_z \\ \boldsymbol{I}_{n_s \times n_s} & \boldsymbol{0}_{n_s \times n_s} & \boldsymbol{0}_{n_s \times 4n_a} \\ \boldsymbol{B}_{\dot{z}}\boldsymbol{H}_{as} & \boldsymbol{B}_z\boldsymbol{H}_{as} & \boldsymbol{A}_z \end{bmatrix} \times \begin{bmatrix} \dot{\boldsymbol{x}}_s \\ \boldsymbol{x}_s \\ \boldsymbol{z}_a \end{bmatrix} + \begin{bmatrix} \boldsymbol{M}_{ae}^{-1}\boldsymbol{H}_u \\ \boldsymbol{0}_{n_s \times 1} \\ \boldsymbol{0}_{4n_a \times 1} \end{bmatrix} \boldsymbol{u}_w + \begin{bmatrix} \boldsymbol{0}_{n_s \times n_a} \\ \boldsymbol{0}_{n_s \times n_a} \\ \boldsymbol{B}_{zg} \end{bmatrix} \boldsymbol{\alpha}_g + \begin{bmatrix} \boldsymbol{M}_{ae}^{-1}\boldsymbol{F}_{s,\text{grav}} \\ \boldsymbol{0}_{n_s \times 1} \\ \boldsymbol{0}_{4n_a \times 1} \end{bmatrix} + \begin{bmatrix} \boldsymbol{M}_{ae}^{-1}\boldsymbol{H}_{sa}\boldsymbol{K}_{zr} \\ \boldsymbol{0}_{n_s \times n_a} \\ \boldsymbol{B}_{zr} \end{bmatrix} \boldsymbol{\alpha}_{qs,r} + \begin{bmatrix} \boldsymbol{M}_{ae}^{-1}\boldsymbol{F}_{s,\text{acc}} \\ \boldsymbol{0}_{n_s \times 1} \\ \boldsymbol{0}_{4n_a \times 1} \end{bmatrix} \tag{3}$$

in which $\boldsymbol{M}_{ae} = \boldsymbol{M}_{s,n_s} - \boldsymbol{H}_{sa}\boldsymbol{M}_a\boldsymbol{H}_{as}$. Recall Eq. (1); the wing root reaction force is calculated as

$$\begin{aligned} \boldsymbol{F}_{\text{root}} &= \boldsymbol{M}_{s,1}\ddot{\boldsymbol{x}}_s + \boldsymbol{K}_{s,1}\boldsymbol{x}_s = \boldsymbol{M}_{s,1}\boldsymbol{M}_{ae}^{-1}\boldsymbol{H}_{sa}\boldsymbol{K}_{zr}\boldsymbol{\alpha}_{qs,r} + \boldsymbol{M}_{s,1}\boldsymbol{M}_{ae}^{-1}(\boldsymbol{H}_u\boldsymbol{u}_w + \boldsymbol{F}_{s,\text{acc}} + \boldsymbol{F}_{s,\text{grav}}) \\ &\quad + \begin{bmatrix} \boldsymbol{M}_{s,1}\boldsymbol{M}_{ae}^{-1}\boldsymbol{H}_{sa}\boldsymbol{C}_a\boldsymbol{H}_{as} & \boldsymbol{M}_{s,1}\boldsymbol{M}_{ae}^{-1}(\boldsymbol{H}_{sa}\boldsymbol{K}_a\boldsymbol{H}_{as} - \boldsymbol{K}_{s,n_s}) + \boldsymbol{K}_{s,1} & \boldsymbol{M}_{s,1}\boldsymbol{M}_{ae}^{-1}\boldsymbol{H}_{sa}\boldsymbol{K}_z \end{bmatrix} \begin{bmatrix} \dot{\boldsymbol{x}}_s^\intercal & \boldsymbol{x}_s^\intercal & \boldsymbol{z}_a^\intercal \end{bmatrix}^\intercal \end{aligned} \tag{4}$$

Define the lag state vector as $\boldsymbol{z}_a \in \mathbb{R}^{4n_a}$, the aerodynamic state vector as $\boldsymbol{x}_a \in \mathbb{R}^{3n_a}$, and the aerodynamic output vector as $\boldsymbol{f}_{\text{aero}} = [\boldsymbol{f}_{\text{aero},1}^\intercal, \ldots, \boldsymbol{f}_{\text{aero},n_a}^\intercal]^\intercal$, then

$$\begin{aligned} \dot{\boldsymbol{z}}_a &= \boldsymbol{A}_z\boldsymbol{z}_a + \boldsymbol{B}_z\boldsymbol{x}_a + \boldsymbol{B}_{\dot{z}}\dot{\boldsymbol{x}}_a + \boldsymbol{B}_{zr}\boldsymbol{\alpha}_{qs,r} + \boldsymbol{B}_{zg}\boldsymbol{\alpha}_g, \\ \boldsymbol{f}_{\text{aero}} &= \boldsymbol{M}_a\ddot{\boldsymbol{x}}_a + \boldsymbol{C}_a\dot{\boldsymbol{x}}_a + \boldsymbol{K}_a\boldsymbol{x}_a + \boldsymbol{K}_z\boldsymbol{z} + \boldsymbol{K}_{zr}\boldsymbol{\alpha}_{qs,r} \end{aligned} \tag{2}$$

where $\boldsymbol{\alpha}_{qs,r} \in \mathbb{R}^{n_a}$ and $\boldsymbol{\alpha}_g \in \mathbb{R}^{n_a}$ are the angle-of-attack vectors induced by rigid-body motions and gusts. The aerodynamic mass, damping, and stiffness matrices are denoted as $\boldsymbol{M}_a$, $\boldsymbol{C}_a$, and $\boldsymbol{K}_a$, respectively. They include both noncirculatory and circulatory effects.

The gravitational force and moment per unit length expressed in $\mathcal{F}_W$ are $\boldsymbol{f}_{\text{grav}} = \iint_{A_w} \boldsymbol{C}_{WB}\boldsymbol{C}_{BI}[0, 0, \rho g]^\intercal \, \mathrm{d}r_x \, \mathrm{d}r_z$ and $\boldsymbol{m}_{\text{grav}} = \iint_{A_w} ([0, r_y, r_z]^\intercal + \boldsymbol{r}_e) \times \boldsymbol{C}_{WB}\boldsymbol{C}_{BI}[0, 0, \rho g]^\intercal \, \mathrm{d}r_x \, \mathrm{d}r_z$, where g is the gravitational acceleration and $\boldsymbol{r}_e$ is the elastic deformation vector (Appendix A). The matrices $\boldsymbol{C}_{WB}$ and $\boldsymbol{C}_{BI}$ denote the direction cosine matrices from the body frame to $\mathcal{F}_W$, and from the inertial frame $\mathcal{F}_I$ (O_I, x_I, y_I, z_I) (Fig. 1) to the body frame, respectively. These distributed forces and moments are integrated to their nearest structural node, leading to $\boldsymbol{F}_{\text{s,grav}} = [[f_w, f_\phi, f_\theta, f_\beta]_{\text{grav},1}, \ldots, [f_w, f_\phi, f_\theta, f_\beta]_{\text{grav},n_s}]^\intercal \in \mathbb{R}^{4n_s}$.

The actuation moment around the hinge is chosen as the control input, which is more physically meaningful than the flap angle itself. Denote the actuation moment for the ith flap as u_i, then the input vector is $\boldsymbol{u}_w = [u_1, \ldots, u_{n_s}]^\intercal \in \mathbb{R}^{n_s}$. Moreover, $\boldsymbol{F}_{s,\text{act}} =$

The preceding wing aeroservoelastic model is derived in a modular approach. The control input, atmospheric disturbance, gravitational force, and the rigid-body motion-induced aerodynamic angle and inertial force are modeled as separate inputs to the system. This allows convenient contribution assessments of different factors on the dynamic loads. Furthermore, this approach provides a clear interface between the conventional clamped-wing aeroservoelastic dynamics and the free-flying wing aeroservoelastic dynamics. If $\boldsymbol{F}_{s,\text{acc}}$ and $\boldsymbol{\alpha}_{qs,r}$ are set to zero, while the orientation matrices in $\boldsymbol{F}_{s,\text{grav}}$ are evaluated at the trimmed condition, then Eqs. (3) and (4) degenerate to the conventional clamped-wing aeroservoelastic dynamics. Conversely, no matter how the aerodynamics and structural dynamics are modeled and coupled (finite-element method, panel method, etc.), as long as the resulting aeroelastic model can be written in the state-space form, the clamped-wing model can be made free-flying by adding $\boldsymbol{F}_{s,\text{acc}}$, $\boldsymbol{\alpha}_{qs,r}$, and the direction cosine matrices.

B. Free-Flying Dynamics of the Flexible Aircraft

Define $\boldsymbol{V}_b = [V_x, V_y, V_z]^\intercal$ and $\boldsymbol{\omega}_b = [p, q, r]^\intercal$ as the translational and rotational velocities of $\mathcal{F}_B$. Also define $\boldsymbol{a}_b = [a_x, a_y, a_z]^\intercal$ and $\boldsymbol{\alpha}_b = [\dot{p}, \dot{q}, \dot{r}]^\intercal$ as the translational and rotational accelerations of $\mathcal{F}_B$. These four vectors are all expressed in $\mathcal{F}_B$. Denote V as the ground velocity, γ as the flight path angle, and χ as the kinematic azimuth angle, then the flexible aircraft translational dynamics expressed in the flight trajectory axes are

$$\begin{bmatrix}\dot{V} & \dot{\chi} & \dot{\gamma}\end{bmatrix}^{\intercal} = \boldsymbol{G}_V \frac{\boldsymbol{C}_{VB}}{m}(\boldsymbol{F}^B_{\text{tot}} - \tilde{\boldsymbol{S}}^{\intercal}\boldsymbol{\alpha}_b - m\tilde{\boldsymbol{\omega}}_b\boldsymbol{V}_b - \tilde{\boldsymbol{\omega}}_b\tilde{\boldsymbol{S}}^{\intercal}\boldsymbol{\omega}_b + \boldsymbol{d}_F) \quad (5)$$

where

$$\boldsymbol{G}_V = \text{diag}\left(\left[1, \frac{1}{V\cos\gamma}, -\frac{1}{V}\right]\right)$$

The rotational dynamics of the aircraft expressed in the body-fixed frame $\mathcal{F}_B$ are

$$\boldsymbol{J}\dot{\boldsymbol{\omega}}_b = -\tilde{\boldsymbol{S}}\dot{\boldsymbol{V}}_b - \tilde{\boldsymbol{V}}_b\tilde{\boldsymbol{S}}^{\intercal}\boldsymbol{\omega}_b - \tilde{\boldsymbol{\omega}}_b\tilde{\boldsymbol{S}}\boldsymbol{V}_b - \tilde{\boldsymbol{\omega}}_b\boldsymbol{J}\boldsymbol{\omega}_b + \boldsymbol{M}^B_{\text{tot}} + \boldsymbol{d}_M \quad (6)$$

The vectors $\boldsymbol{F}^B_{\text{tot}}$ and $\boldsymbol{M}^B_{\text{tot}}$ denote the total external forces and moments expressed in $\mathcal{F}_B$, which contain aerodynamic, gravitational, and propulsion forces. The first and second moment of inertia matrices are $\tilde{\boldsymbol{S}}$ and $\boldsymbol{J}$, respectively. Their specific expressions are shown in Appendix B. The vectors $\boldsymbol{d}_F$ and $\boldsymbol{d}_M$ are functions of elastic accelerations and cross couplings between rigid-body and elastic velocities. Their expressions are also shown in Appendix B. If $\boldsymbol{d}_F$ and $\boldsymbol{d}_M$ are set to zero, while $\boldsymbol{S}$ and $\boldsymbol{J}$ are kept constant, then the rigid-body dynamics are retrieved. If in the resulting simplified dynamics, further set $\boldsymbol{S}$ to zero, then the conventional rigid-body dynamics where O_b is coincide with aircraft center of mass are retrieved. The nonzero vectors $\boldsymbol{d}_F$ and $\boldsymbol{d}_M$ and the dependencies of $\boldsymbol{S}$ and $\boldsymbol{J}$ on elastic states essentially reflect the inertial couplings between rigid-body and elastic motions.

As compared with the inertial couplings, aerodynamic couplings normally have more dominant effects. On the one hand, rigid-body motions excite wing aeroelastic dynamics through the input $\boldsymbol{\alpha}_{qs,r}$. On the other hand, $\boldsymbol{F}^B_{\text{tot}}$ and $\boldsymbol{M}^B_{\text{tot}}$ are contributed by $\boldsymbol{f}_{\text{aero}}$, which is a function of aeroelastic states. The conventional mean-axes method only considers aerodynamic couplings [24]. In Eq. (2), drag is not considered in $\boldsymbol{f}_{\text{aero}}$, whereas it should be integrated to $\boldsymbol{F}^B_{\text{tot}}$ and $\boldsymbol{M}^B_{\text{tot}}$. The quasi-steady strip theory is used for the distributed lift and drag on fuselage and tails. Denote the distance vector from O_b to an arbitrary strip as $\boldsymbol{r}_i$ (expressed in $\mathcal{F}_B$), then the local airspeed is $\boldsymbol{V}_{a_i} = \boldsymbol{V}_b + \tilde{\boldsymbol{\omega}}_b\boldsymbol{r}_i - \boldsymbol{C}_{BI}[0, 0, w_g(t)]^{\intercal}$. The local dynamic pressure and aerodynamic angles are then calculated from $\boldsymbol{V}_{a_i}$. During simulations, the disturbance velocity $w_g(t)$ is calculated by interpolating the spatial vertical atmospheric disturbance field at the local strip position $\boldsymbol{R}_b + \boldsymbol{C}^{\intercal}_{BI}\boldsymbol{r}_i$, where the distance vector $\boldsymbol{R}_b$ is defined in Fig. 1.

III. Control Design

After presenting the wing aeroservoelastic dynamics and flight dynamics, the flexible aircraft trajectory tracking control architecture will be proposed in this section. Cascaded loops are widely adopted in flexible aircraft control [25,26]. The control architecture presented in this paper contains four cascaded loops: position control, flight path control, attitude control, and optimal multi-objective wing control. These loops will be designed in the following subsections.

A. Position Control

Define the distance vector from O_I to O_b expressed in the inertial frame as $\boldsymbol{R}_b = [X, Y, Z]^{\intercal}$ (Fig. 1), then the translational kinematics are $\dot{X} = V\cos\chi\cos\gamma, \dot{Y} = V\sin\chi\cos\gamma, \dot{Z} = -V\sin\gamma$. The control objective is to make the aircraft follow a predesigned three-dimensional trajectory $[X^{\text{ref}}, Y^{\text{ref}}, Z^{\text{ref}}]^{\intercal}$. Because there is no model uncertainty in these kinematics, the NDI control is adopted. Design the virtual controls as $\nu_Y = \dot{Y}^{\text{ref}} + K_Y(Y^{\text{ref}} - Y), \nu_Z = \dot{Z}^{\text{ref}} + K_Z(Z^{\text{ref}} - Z)$, where K_Y and K_Z are positive gains, then when $\dot{Y} = \nu_Y$ and $\dot{Z} = \nu_Z$, the lateral and vertical tracking errors converge to zero *exponentially*. If $\dot{Y}^{\text{ref}}$ and $\dot{Z}^{\text{ref}}$ are not available, then they can be omitted from the virtual control design. Even so, the resulting tracking errors would still converge *asymptomatically*. Replace $\dot{Y}$ and $\dot{Z}$ by their virtual controls, and invert the resulting equations, then the references for the kinematic azimuth angle and the flight path angle are

$$\chi^{\text{ref}} = \arcsin(\nu_Y/(V\cos\gamma)), \qquad \gamma^{\text{ref}} = -\arcsin(\nu_Z/V) \quad (7)$$

B. Flight Path Control

The control objective of this loop is to make the flight path angles track their references designed in Eq. (7). Define the aerodynamic axes as $\mathcal{F}_A$ (O_b, x_A, y_A, z_A), where $O_b x_A$ is aligned with the aircraft airspeed vector, and $O_b z_A$ pointing downward in the aircraft symmetrical plane. Use $\boldsymbol{C}_{ij}$ to denote the direction cosine matrix from the reference frame $\mathcal{F}_j$ to the reference frame $\mathcal{F}_i$. Consequently, the aircraft translational dynamics given in Eq. (5) are rewritten as

$$\begin{bmatrix}\dot{V}\\ \dot{\chi}\\ \dot{\gamma}\end{bmatrix} = \begin{bmatrix}1 & 0 & 0\\ 0 & \frac{1}{V\cos\gamma} & 0\\ 0 & 0 & -\frac{1}{V}\end{bmatrix} \left(\frac{\boldsymbol{C}_{VB}}{m}\begin{bmatrix}T\\0\\0\end{bmatrix} + \frac{\boldsymbol{C}_{VI}}{m}\begin{bmatrix}0\\0\\mg\end{bmatrix} + \frac{\boldsymbol{C}_{VA}}{m}\begin{bmatrix}-D\\C\\-L\end{bmatrix} + \begin{bmatrix}d_1\\d_2\\d_3\end{bmatrix}\right) \quad (8)$$

in which $[T, 0, 0]^{\intercal}$ is the thrust vector. The total drag, side force, and lift defined in $\mathcal{F}_A$ are, respectively, denoted by D, C, and L. Moreover, using Eq. (5), $[d_1, d_2, d_3]^{\intercal}$ equals $(\boldsymbol{C}_{VB}/m)(-\tilde{\boldsymbol{S}}^{\intercal}\boldsymbol{\alpha}_b - m\tilde{\boldsymbol{\omega}}_b\boldsymbol{V}_b - \tilde{\boldsymbol{\omega}}_b\tilde{\boldsymbol{S}}^{\intercal}\boldsymbol{\omega}_b + \boldsymbol{d}_F)$ Substituting the expressions of the direction cosine matrices into Eq. (8), then the flight path angle dynamics are

$$\dot{\gamma} = -\frac{1}{mV}(-T\sin\alpha\cos\mu + mg\cos\gamma - L\cos\mu + d_3) \quad (9)$$

From a physical point of view, one of the most effective ways of changing aircraft flight path is to modify the total lift, which is dominated by the angle of attack α. Therefore, α is selected as a control input to the dynamics of γ, which is denoted as u_α. In this flight path control loop, define $\boldsymbol{x} = [\dot{\boldsymbol{x}}^{\intercal}_s, \boldsymbol{x}^{\intercal}_s, \boldsymbol{x}^{\intercal}_a, \boldsymbol{z}^{\intercal}_a, \boldsymbol{V}^{\intercal}_b, \boldsymbol{\omega}^{\intercal}_b, \boldsymbol{R}^{\intercal}_b, V, \chi, \gamma, \mu, \beta]^{\intercal}$, then Eq. (9) is represented by

$$\dot{\gamma} = f_\gamma(\boldsymbol{x}, u_\alpha) + d_\gamma \quad (10)$$

where $f_\gamma(\boldsymbol{x}, u_\alpha) = -(1/mV)(-T\sin\alpha\cos\mu + mg\cos\gamma - L\cos\mu)$ and $d_\gamma = -d_3/(mV)$. It can be seen that Eq. (10) is nonaffine in control. Conventional nonlinear control methods, including feedback linearization and backstepping, cannot be directly applied. In this paper, the novel incremental sliding mode control method is adopted, which not only applies to nonaffine in control systems, but also has enhanced robustness to model uncertainties [19].

Design the sliding surface as $\sigma_\gamma = \gamma - \gamma^{\text{ref}}$. The control objective is to design a reference for α, such that when α tracks its reference through inner-loop control, σ_γ also converges to zero. Denote the sampling interval as Δt, the incremental dynamic equation is derived by taking the first-order Taylor series expansion of Eq. (10) around the condition at $t - \Delta t$ (denoted by the subscript 0) as

$$\begin{aligned}\dot{\gamma} &= f_\gamma(\boldsymbol{x}, u_\alpha) + d_\gamma = \dot{\gamma}_0 + \Delta f_\gamma + \Delta d_\gamma\\ &= \dot{\gamma}_0 + \left.\frac{\partial f_\gamma}{\partial u_\alpha}\right|_0 \Delta u_\alpha + \left.\frac{\partial f_\gamma}{\partial \boldsymbol{x}}\right|_0 \Delta\boldsymbol{x} + \Delta d_\gamma + R_1\end{aligned} \quad (11)$$

in which $\Delta\boldsymbol{x}$ and Δu_α, respectively, represents the variations of $\boldsymbol{x}$ and u_α in one sampling time step Δt. The expansion remainder of f_γ is R_1, whose Lagrange form is

$$R_1 = \frac{1}{2}\left.\frac{\partial^2 f_\gamma}{\partial^2 \boldsymbol{x}}\right|_m \Delta\boldsymbol{x}^2 + \left.\frac{\partial^2 f_\gamma}{\partial\boldsymbol{x}\partial u_\alpha}\right|_m \Delta\boldsymbol{x}\Delta u_\alpha + \frac{1}{2}\left.\frac{\partial^2 f_\gamma}{\partial^2 u_\alpha}\right|_m \Delta u_\alpha^2$$

in which $(\cdot)|_m$ means evaluating $(\cdot)$ at a condition where $\boldsymbol{x} \in (\boldsymbol{x}(t-\Delta t), \boldsymbol{x}(t))$ and $u_\alpha \in (u_\alpha(t-\Delta t), u_\alpha(t))$. The variation of d_γ in Δt is denoted as Δd_γ, which is also a function of $\Delta \boldsymbol{x}$ and Δu_α. Because a change in α has more dominate impacts on f_γ than on d_γ, the partial derivative of f_γ with respect to u_α is considered as the dominate control effectiveness. The term Δd_γ is considered as a perturbation term and will be observed and compensator for by sliding mode virtual control.

The incremental sliding mode control law for stabilizing σ_γ is then designed as

$$\Delta u_\alpha = (\nu_n + \nu_s + \dot{\gamma}^{\text{ref}} - \dot{\gamma}_0)/\bar{G}_0 \tag{12}$$

where the virtual control ν_n is designed to stabilize the nominal sliding mode dynamics, whereas ν_s is a robust virtual control for disturbance rejection. The real control input equals $\Delta u_\alpha + u_{\alpha,0}$, where $u_{\alpha,0}$ denotes the control input at $t - \Delta t$. In Eq. (12), $\bar{G}_0$ represents the estimation of the control effectiveness

$$\left.\frac{\partial f_\gamma}{\partial u_\alpha}\right|_0$$

It can be seen from Eq. (9) that

$$G_0 = \left.\frac{\partial f_\gamma}{\partial u_\alpha}\right|_0 = \left.\frac{\cos\mu}{mV}\left(T\cos\alpha + \frac{\partial L}{\partial \alpha}\right)\right|_0$$

Its estimation is calculated as $\bar{G}_0 = (\cos\mu/mV)(T\cos\alpha + q_\infty S_w \bar{C}_{L\alpha})|_0$ where q_∞ is the dynamic pressure and S_w is the wing area. Substituting Eq. (12) into Eq. (11), then the closed-loop dynamics are

$$\begin{aligned}\dot{\sigma}_\gamma = \dot{\gamma} - \dot{\gamma}^{\text{ref}} &= \dot{\gamma}_0 + (G_0/\bar{G}_0)(\nu_n + \nu_s + \dot{\gamma}^{\text{ref}} - \dot{\gamma}_0) - \dot{\gamma}^{\text{ref}} \\ &\quad + \delta(\boldsymbol{x}, \Delta t) + \Delta d_\gamma \triangleq \nu_n + \nu_s + \varepsilon_\gamma\end{aligned} \tag{13}$$

where $\delta(\boldsymbol{x}, t)$ is the closed-loop value of the state variations and the expansion reminder:

$$\delta(\boldsymbol{x}, t) = \left[\left.\frac{\partial f_\gamma}{\partial \boldsymbol{x}}\right|_0 \Delta \boldsymbol{x} + R_1\right]_{u_\alpha = u_{\alpha,0} + \Delta u_\alpha}$$

In Eq. (13), ε_γ is the lumped perturbation term, which is expressed as

$$\varepsilon_\gamma = \delta(\boldsymbol{x}, \Delta t) + \Delta d_\gamma + (G_0/\bar{G}_0 - 1)(\nu_n + \nu_s + \dot{\gamma}^{\text{ref}} - \dot{\gamma}_0) \tag{14}$$

Assumption 1: The $\delta(\boldsymbol{x}, \Delta t)$ in Eq. (13) and the Δd_γ in Eq. (11) satisfy $|\delta(\boldsymbol{x}, \Delta t)| < \bar{\delta}$ and $|\Delta d_\gamma| < \bar{d}_\gamma$.

The dynamics of $\boldsymbol{x}$ are governed by first-order differentiable equations [Eqs. (3), (5), and (6)]. Because $\boldsymbol{x}$ is continuously differentiable, then $\lim_{\Delta t \to 0} \|\Delta \boldsymbol{x}\| = 0$ [16,19]. If the partial derivatives of f_γ with respect to $\boldsymbol{x}$, up to any order, are bounded, then in view of Eq. (13) and the expression of R_1, the absolute value of $\delta(\boldsymbol{x}, \Delta t)$ approaches zero as Δt decreases. Therefore, this assumption holds when Δt is sufficiently small.

Proposition 1: Under Assumption 1, if $0 < G_0/\bar{G}_0 < 2$, then when the sampling frequency f_s is sufficient high, the uncertainty term ε_γ in Eq. (14) is ultimately bounded.

Proof: Substitute Eq. (12) into Eq. (11), then the resulting closed-loop dynamics are $\dot{\gamma} = \nu_n + \nu_s + \dot{\gamma}^{\text{ref}} + \varepsilon_\gamma$. This equation is also valid at $t - \Delta t$; thus $\dot{\gamma}_0 = (\nu_n + \nu_s + \dot{\gamma}^{\text{ref}})|_0 + \varepsilon_{\gamma,0}$. Therefore, ε_γ in Eq. (14) is rewritten as

$$\begin{aligned}\varepsilon_\gamma &= \delta(\boldsymbol{x}, \Delta t) + \Delta d_\gamma + (G_0/\bar{G}_0 - 1)(\nu_n + \nu_s + \dot{\gamma}^{\text{ref}} \\ &\quad - ((\nu_n + \nu_s + \dot{\gamma}^{\text{ref}})|_0 + \varepsilon_{\gamma,0})) \\ &= (1 - G_0/\bar{G}_0)\varepsilon_{\gamma,0} - (1 - G_0/\bar{G}_0)(\nu_\gamma - \nu_{\gamma,0}) + \delta(\boldsymbol{x}, \Delta t) + \Delta d_\gamma\end{aligned} \tag{15}$$

where $\nu_\gamma = \nu_n + \nu_s + \dot{\gamma}^{\text{ref}}$. These virtual control terms are all continuous in time; thus under sufficiently high sampling frequency, the variation of ν_γ in Δt has an upper bound, i.e., $|\nu_\gamma - \nu_{\gamma,0}| < \bar{\nu}_\gamma$. Analogous to the proof of Theorem 1 in [19], the ultimate boundedness of ε_γ can be proved. □

The boundedness of ε_γ makes it feasible to compensate for its influences using robust control. In this paper, ν_s in Eq. (12) is designed using a super-twisting sliding mode disturbance observer. Design an auxiliary sliding variable as $s_\gamma = \sigma_\gamma - \int \nu_n \, \mathrm{d}t$, then using Eq. (13), the dynamics of s_γ are $\dot{s}_\gamma = \dot{\sigma}_\gamma - \nu_n = \nu_s + \varepsilon_\gamma$. Further design the observer virtual control as $\nu_s = -\lambda_\gamma |s_\gamma|^{0.5} \operatorname{sign}(s_\gamma) - \beta_\gamma \int \operatorname{sign}(s_\gamma)\, \mathrm{d}t$. Denote the upper bound of ε_γ as $\bar{\varepsilon}_\gamma$, and design $\lambda_\gamma = 1.5\bar{\varepsilon}_\gamma^{0.5}$ and $\beta = 1.1\bar{\varepsilon}_\gamma$, then $s_\gamma = \dot{s}_\gamma = 0$ is established in finite time [27]. On this sliding surface, ν_s provides a real-time observation of the uncertainty term $-\varepsilon_\gamma$. Moreover, the nominal dynamics $\dot{\sigma}_\gamma = \nu_n$ are retrieved regardless of uncertainties. Design the nominal virtual control as $\nu_n = -K_\sigma \sigma_\gamma$, with $K_\sigma > 0$, then σ_γ converges to zero exponentially. The observer gains can also be made adaptive, which removes the per-knowledge requirement on the uncertainty bound [27].

Remark 1: The only model information required by the incremental sliding mode control in Eq. (12) is the control effectiveness G_0. In the flight path control loop, the model parameters in G_0 are only the wing area S_w and the aircraft lift-slope $C_{L\alpha}$. These two parameters are easily known from aircraft overall design. The other variables needed to calculate $\bar{G}_0$ can be either directly sensed or indirectly calculated from onboard sensor measurements. Therefore, it is reasonable to assume that $\bar{G}_0$ is close to G_0; i.e., $0 < G_0/\bar{G}_0 < 2$. Furthermore, since $\bar{G}_0$ is used as the denominator of the control law, its singularity has to be discussed. The situation $\bar{G}_0 = 0$ happens when

$$\bar{C}_{L\alpha} = \left.\frac{-T\cos\alpha}{q_\infty S_w}\right|_0$$

indicating that the lift slope has to become negative, which only happens in stall condition. Nevertheless, preventing the aircraft from stall and enforcing α to track α_{ref} are the objectives of the inner-loop attitude control.

Remark 2: The proposed flight path control differs from the one in [28] in three aspects:

1) The residual uncertainty term ε_γ is observed and is compensated for in this paper.

2) In Eq. (8), the aerodynamic forces are expressed in the aerodynamic axes, whereas in [28], they are expressed in the body axes. Consequently, the aerodynamic coefficient used in the proposed controller is only $C_{L\alpha}$, whereas Ref. [28] requires both $C_{X\alpha}$ and $C_{Z\alpha}$ (X, Z are the aerodynamic forces expressed in the body-fixed frame). As compared with $C_{X\alpha}$ and $C_{Z\alpha}$, the state dependency of $C_{L\alpha}$ is much lower, which simplifies the identification process and enhances robustness.

3) In Ref. [28], throttle control is also included in the incremental control loop. However, aircraft throttle normally has much lower bandwidth than the aerodynamic control surfaces. In view of this, a separate throttle controller (δ_T) for maintaining airspeed is adopted in this paper.

After presenting the flight path angle (γ) control law, the reference tracking problem for the kinematic azimuth angle χ will be solved. Recall Eq. (8); the dynamics are

$$\dot{\chi} = \frac{1}{V\cos\gamma}(T\sin\alpha\cos\mu + L\sin\mu + d_2)$$

Choose the kinematic bank angle μ as the control input. Replace $\dot{\gamma}$ and $\dot{\chi}$ by their virtual control ν_γ and ν_χ, respectively, and then invert the resulting dynamics; the reference for μ is designed as

$$\mu^{\text{ref}} = \arctan\left(\frac{\nu_\chi V\cos\gamma}{\nu_\gamma V + g\cos\gamma}\right)$$

in which ν_γ has been designed in the preceding texts, whereas the virtual control ν_χ is designed as $\nu_\chi = \dot{\chi}^{\text{ref}} + K_\chi(\chi^{\text{ref}} - \chi)$ with $K_\chi > 0$.

C. Attitude Control

The objective of this attitude control loop is to make μ, α, and β track their references; μ^{ref} and α^{ref} have been designed in Sec. III.B. The β^{ref} is set to zero for mitigating side force. From a physical point of view, the attitude of an aircraft can be changed by creating control moments around $O_b x_b$, $O_b y_b$, and $O_b z_b$ axes. For the configuration shown in Fig. 1, the elevator δ_e and rudder δ_r can generate pitch and yaw control moments. On the other hand, the difference between the left and right wing root bending moments $M_{\phi,\text{diff}} = M_{\phi,l} - M_{\phi,r}$ is essentially the main source of aircraft rolling moment. These bending moments can be extracted from strain measurements at a sampling frequency around 1 kHz.

Define the state vectors as $\boldsymbol{x}_1 = [\mu, \alpha, \beta]^\intercal$ and $\boldsymbol{x}_2 = [p, q, r]^\intercal$, and define the control vector as $\boldsymbol{u} = [\delta_e, \delta_r, M_{\phi,\text{diff}}]^\intercal$, then the attitude kinematics [29] and dynamics [Eq. (6)] can be represented as $\dot{\boldsymbol{x}}_1 = \boldsymbol{f}_1(\boldsymbol{x}_1) + \boldsymbol{G}_1(\boldsymbol{x}_1)\boldsymbol{x}_2$ and $\dot{\boldsymbol{x}}_2 = \boldsymbol{f}_2(\boldsymbol{x}_1, \boldsymbol{x}_2, \boldsymbol{x}_e) + \boldsymbol{G}_2(\boldsymbol{x}_1, \boldsymbol{x}_2, \boldsymbol{x}_e, \boldsymbol{u}) + \boldsymbol{d}$, where $\boldsymbol{d} = \boldsymbol{J}^{-1}\boldsymbol{d}_M$, whereas $\boldsymbol{x}_e = [\dot{\boldsymbol{x}}_s, \boldsymbol{x}_s, z_a]^\intercal$ represents the state vector in Eq. (3). Choose the controlled output as $\boldsymbol{y} = \boldsymbol{x}_1$. In view of the attitude kinematics [29], there is no model uncertainty in $\boldsymbol{f}_1$ and $\boldsymbol{G}_1$. On the contrary, $\boldsymbol{f}_2$ and $\boldsymbol{G}_2$ contain model uncertainties; they are also functions of elastic states. In addition, $\boldsymbol{G}_2$ is nonaffine in control, which makes direct applications of feedback linearization and backstepping infeasible.

The novel incremental backstepping sliding mode control is adopted to handle this output tracking problem. Define the error variable as $\boldsymbol{z}_1 = \boldsymbol{y} - \boldsymbol{y}^{\text{ref}}$, then $\dot{\boldsymbol{z}}_1 = \boldsymbol{f}_1 + \boldsymbol{G}_1\boldsymbol{x}_2 - \dot{\boldsymbol{y}}^{\text{ref}}$. Consider a candidate Lyapunov function $V_1(\boldsymbol{z}_1) = (1/2)\boldsymbol{z}_1^\intercal\boldsymbol{z}_1$. To make $\dot{V}_1(\boldsymbol{z}_1) \le 0$, the reference for $\boldsymbol{x}_2$ is designed as $\boldsymbol{x}_2^{\text{ref}} = \boldsymbol{G}_1^{-1}(-\boldsymbol{f}_1 - \boldsymbol{K}_1\boldsymbol{z}_1 + \dot{\boldsymbol{y}}^{\text{ref}})$, in which $\boldsymbol{K}_1$ is a positive definite gain matrix. Further define $\boldsymbol{z}_2 = \boldsymbol{x}_2 - \boldsymbol{x}_2^{\text{ref}}$, then the resulting dynamics are $\dot{\boldsymbol{z}}_2 = \boldsymbol{f}_2(\boldsymbol{x}_1, \boldsymbol{x}_2, \boldsymbol{x}_e) + \boldsymbol{G}_2(\boldsymbol{x}_1, \boldsymbol{x}_2, \boldsymbol{x}_e, \boldsymbol{u}) + \boldsymbol{d} - \dot{\boldsymbol{x}}_2^{\text{ref}}$. Denote the augmented state vector as $\boldsymbol{x} = [\boldsymbol{x}_1^\intercal, \boldsymbol{x}_2^\intercal, \boldsymbol{x}_e^\intercal]^\intercal$. The incremental dynamics of $\boldsymbol{x}_2$ are derived by taking the first-order Taylor series expansion around the condition at $t - \Delta t$ (denoted by the subscript 0) as

$$\dot{\boldsymbol{x}}_2 = \dot{\boldsymbol{x}}_{2,0} + \left.\frac{\partial[\boldsymbol{f}_2(\boldsymbol{x}) + \boldsymbol{G}_2(\boldsymbol{x},\boldsymbol{u})]}{\partial \boldsymbol{u}}\right|_0 \Delta\boldsymbol{u} + \left.\frac{\partial[\boldsymbol{f}_2(\boldsymbol{x}) + \boldsymbol{G}_2(\boldsymbol{x},\boldsymbol{u})]}{\partial \boldsymbol{x}}\right|_0 \Delta\boldsymbol{x} + \Delta\boldsymbol{d} + \boldsymbol{R}_1' \tag{16}$$

where $\Delta\boldsymbol{x} = \boldsymbol{x} - \boldsymbol{x}_0$, $\Delta\boldsymbol{u} = \boldsymbol{u} - \boldsymbol{u}_0$, and $\Delta\boldsymbol{d} = \boldsymbol{d} - \boldsymbol{d}_0$, respectively, denote the variations of states, control inputs, and disturbances, in one incremental time step. The term $\boldsymbol{R}_1'$ in Eq. (16) is the expansion remainder, whose Lagrange form is

$$\boldsymbol{R}_1' = \frac{1}{2}\left.\frac{\partial^2[\boldsymbol{f}_2(\boldsymbol{x}) + \boldsymbol{G}_2(\boldsymbol{x},\boldsymbol{u})]}{\partial^2 \boldsymbol{x}}\right|_m \Delta\boldsymbol{x}^2 + \left.\frac{\partial^2[\boldsymbol{f}_2(\boldsymbol{x}) + \boldsymbol{G}_2(\boldsymbol{x},\boldsymbol{u})]}{\partial \boldsymbol{x}\partial \boldsymbol{u}}\right|_m \Delta\boldsymbol{x}\Delta\boldsymbol{u} + \frac{1}{2}\left.\frac{\partial^2[\boldsymbol{f}_2(\boldsymbol{x}) + \boldsymbol{G}_2(\boldsymbol{x},\boldsymbol{u})]}{\partial^2 \boldsymbol{u}}\right|_m \Delta\boldsymbol{u}^2$$

in which $(\cdot)|_m$ means evaluating $(\cdot)$ at a condition where $\boldsymbol{x} \in (\boldsymbol{x}(t - \Delta t), \boldsymbol{x}(t))$, $\boldsymbol{u} \in (\boldsymbol{u}(t - \Delta t), \boldsymbol{u}(t))$, and $\boldsymbol{d} \in (\boldsymbol{d}(t - \Delta t), \boldsymbol{d}(t))$. To stabilize $\boldsymbol{z}_2$, the incremental backstepping sliding mode control input is designed as

$$\Delta\boldsymbol{u}_{\text{ibsmc}} = \bar{\boldsymbol{G}}_2^{-1}(\boldsymbol{\nu}_c + \boldsymbol{\nu}_s - \dot{\boldsymbol{x}}_{2,0}) \tag{17}$$

where $\bar{\boldsymbol{G}}_2$ is the estimation of the control effectiveness matrix

$$\boldsymbol{G}_2 = \left.\frac{\partial[\boldsymbol{f}_2(\boldsymbol{x}) + \boldsymbol{G}_2(\boldsymbol{x},\boldsymbol{u})]}{\partial \boldsymbol{u}}\right|_0$$

The virtual control $\boldsymbol{\nu}_c = -\boldsymbol{K}_2\boldsymbol{z}_2 + \dot{\boldsymbol{x}}_2^{\text{ref}} - \boldsymbol{G}_1^\intercal\boldsymbol{z}_1$ is used for stabilizing the nominal dynamics. The positive definite gain matrix is $\boldsymbol{K}_2$. Consider the sliding surface $\boldsymbol{\sigma} = \boldsymbol{z}_2 = \boldsymbol{0}$, the robust virtual control $\boldsymbol{\nu}_s$ is designed as $\boldsymbol{\nu}_s = -\boldsymbol{K}_s\text{sig}(\boldsymbol{\sigma})^{\gamma_s} = -[K_{s,1}|\sigma_1|^{\gamma_{s,1}}\text{sign}(\sigma_1), K_{s,2}|\sigma_2|^{\gamma_{s,2}}\text{sign}(\sigma_2), K_{s,3}|\sigma_3|^{\gamma_{s,3}}\text{sign}(\sigma_3)]^\intercal$, where $K_{s,i} > 0$, $\gamma_{s,i} \in (0, 1)$. Substituting Eq. (17) into Eq. (16), the closed-loop dynamics are

$$\dot{\boldsymbol{x}}_2 = \boldsymbol{\nu}_c + \boldsymbol{\delta}(\boldsymbol{x}, \Delta t) + (\boldsymbol{G}_2\bar{\boldsymbol{G}}_2^{-1} - \boldsymbol{I})(\boldsymbol{\nu}_c - \dot{\boldsymbol{x}}_{2,0}) + \boldsymbol{G}_2\bar{\boldsymbol{G}}_2^{-1}\boldsymbol{\nu}_s + \Delta\boldsymbol{d} \triangleq \boldsymbol{\nu}_c + \boldsymbol{G}_2\bar{\boldsymbol{G}}_2^{-1}\boldsymbol{\nu}_s + \boldsymbol{\varepsilon}_{\text{ibs}} \tag{18}$$

where $\boldsymbol{\delta}(\boldsymbol{x}, \Delta t)$ equals the summation of the closed-loop values of $\boldsymbol{R}_1'$ and

$$\left.\frac{\partial[\boldsymbol{f}_2(\boldsymbol{x}) + \boldsymbol{G}_2(\boldsymbol{x},\boldsymbol{u})]}{\partial \boldsymbol{x}}\right|_0 \Delta\boldsymbol{x}$$

in Eq. (16).

Proposition 2: If $\|\boldsymbol{I} - \boldsymbol{G}_2\bar{\boldsymbol{G}}_2^{-1}\| \le \bar{b} < 1$ for all t, and if $\|\boldsymbol{\delta}(\boldsymbol{x}, \Delta t)\| \le \bar{\delta}$, $\|\Delta\boldsymbol{d}\| \le \overline{\Delta d}$, then under sufficiently high sampling frequency, $\boldsymbol{\varepsilon}_{\text{ibs}}$ given by Eq. (18) is bounded for all t, and is ultimately bounded by $(\overline{\Delta\nu_c}\bar{b} + \bar{\delta} + \overline{\Delta d})/(1 - \bar{b})$, where $\overline{\Delta\nu_c}$ is the upper bound of $\Delta\boldsymbol{\nu}_c$.

This proposition can be proved following the proofs of the Theorem 1 in [23]. $\|\boldsymbol{I} - \boldsymbol{G}_2\bar{\boldsymbol{G}}_2^{-1}\| \le \bar{b} < 1$ is widely used in adaptive and robust control, which requires a diagonally dominated $\boldsymbol{G}_2\bar{\boldsymbol{G}}_2^{-1}$ [23]. This condition is relatively easy to be satisfied in rigid aircraft control. In a severe damage situation where an F-16 aircraft loses 25% of its right wing, its entire left stabilator, and 50% of its vertical tail, simulation results in [19] show that $\|\boldsymbol{I} - \boldsymbol{G}_2\bar{\boldsymbol{G}}_2^{-1}\| \le \bar{b} < 1$ is still validate under incremental control. For flexible aircraft with low wing torsional stiffness, aileron control reversal can happen, which changes the control directions of $\boldsymbol{G}_2$. An adaptation algorithm can be augmented to incremental sliding mode control to make $\bar{\boldsymbol{G}}_2$ as close as possible to its true value while avoiding the singularity issue caused by sign changes. This can be potentially achieved by using thresholds and the Nussbaum function in the adaptation [30,31]. In this paper, it is assumed that the flexible aircraft operates below its control reversal speed.

Proposition 3: If $\boldsymbol{\varepsilon}_{\text{ibs}}$ [Eq. (18)] is bounded, then the control increment in Eq. (17) makes $\boldsymbol{z}_1$ and $\boldsymbol{z}_2$ ultimately bounded.

Proof: Consider a candidate Lyapunov function $V_2(\boldsymbol{z}_1, \boldsymbol{z}_2) = (1/2)(\boldsymbol{z}_1^\intercal\boldsymbol{z}_1 + \boldsymbol{z}_2^\intercal\boldsymbol{z}_2)$. Using Eq. (17), the condition $\|\boldsymbol{I} - \boldsymbol{G}_2\bar{\boldsymbol{G}}_2^{-1}\| \le \bar{b} < 1$, and the expression of $\dot{\boldsymbol{z}}_1$, the time derivative of V_2 is derived as

$$\begin{aligned}
\dot{V}_2 &= -\boldsymbol{z}_1^\intercal\boldsymbol{K}_1\boldsymbol{z}_1 + \boldsymbol{z}_1^\intercal\boldsymbol{G}_1\boldsymbol{z}_2 + \boldsymbol{z}_2^\intercal(-\boldsymbol{K}_2\boldsymbol{z}_2 - \boldsymbol{G}_1^\intercal\boldsymbol{z}_1 + \boldsymbol{G}_2\bar{\boldsymbol{G}}_2^{-1}\boldsymbol{\nu}_s + \boldsymbol{\varepsilon}_{\text{ibs}}) \\
&= -\boldsymbol{z}_1^\intercal\boldsymbol{K}_1\boldsymbol{z}_1 - \boldsymbol{z}_2^\intercal\boldsymbol{K}_2\boldsymbol{z}_2 + \boldsymbol{z}_2^\intercal(\boldsymbol{\varepsilon}_{\text{ibs}} - \boldsymbol{G}_n\bar{\boldsymbol{G}}_n^{-1}\boldsymbol{K}_s\text{sig}(\boldsymbol{\sigma})^\gamma) \\
&\le -\boldsymbol{z}_1^\intercal\boldsymbol{K}_1\boldsymbol{z}_1 - \boldsymbol{z}_2^\intercal\boldsymbol{K}_2\boldsymbol{z}_2 + \sum_{i=1}^{3}(|\sigma_i\|\varepsilon_{\text{ibs},i}| + (\bar{b} - 1)K_{s,i}|\sigma_i|^{\gamma_{s,i+1}}) \\
&\le -\boldsymbol{z}_1^\intercal\boldsymbol{K}_1\boldsymbol{z}_1 - \boldsymbol{z}_2^\intercal\boldsymbol{K}_2\boldsymbol{z}_2 - \sum_{i=1}^{3}\rho_i|\sigma_i|,\ \forall|\sigma_i| \ge \left(\frac{\rho_i + |\varepsilon_{\text{ibs},i}|}{(1 - \bar{b})K_{s,i}}\right)^{1/(\gamma_{s,i})}, \\
&\quad \forall\rho_i > 0
\end{aligned} \tag{19}$$

which proves that the ultimate bound of σ_i equals

$$\left(\frac{\rho_i + |\varepsilon_{\text{ibs},i}|}{(1 - \bar{b})K_{s,i}}\right)^{1/\gamma_{s,i}}$$

whose size can be made arbitrarily small by increasing $K_{s,i}$ and reducing $\gamma_{s,i}$. Because $\boldsymbol{\sigma} = \boldsymbol{z}_2$, $\boldsymbol{K}_1$ and $\boldsymbol{K}_2$ are positive definite, then both $\boldsymbol{z}_1$ and $\boldsymbol{z}_2$ are ultimately bounded. □

Remark 3: Incremental backstepping sliding mode control has lower model dependency than feedback linearization and backstepping sliding mode control. The only model information needed for implementation is the control effectiveness $\bar{\boldsymbol{G}}_2$. Even so, by virtue of its sensor-based nature, incremental backstepping sliding mode

control actually has enhanced robustness against model uncertainties, sudden actuator faults, and structural damage [23]. Under the same perturbation circumstance, there exists a sampling frequency such that the bound of $\boldsymbol{\varepsilon}_{\text{ibs}}$ is smaller than that of the residual error under backstepping control. This property enables incremental backstepping sliding mode control to passively resist a wider range of perturbations with much lower sliding mode control gains [23].

D. Optimal Multi-Objective Wing Control

In Sec. III.C, the reference values for $\delta_e, \delta_r, M_{\phi,\text{diff}}$ have been designed for aircraft attitude control purposes. The references for δ_e and δ_r can be directly given to the actuators of elevator and rudder, whereas $M^{\text{ref}}_{\phi,\text{diff}}$ still needs to be achieved by aircraft trailing-edge control surfaces. The aircraft model considered in this paper has 14 distributed flaps, which makes the achievement of $M^{\text{ref}}_{\phi,\text{diff}}$ an *over-actuated* problem. As a consequence, after $M^{\text{ref}}_{\phi,\text{diff}}$ is achieved for the purpose of bank angle tracking, the wing system still have *control redundancy* to achieve other objectives. In view of this, an optimal multi-objective wing control law will be designed in this subsection.

The wing-root shear force F_w and wing-root bending moment M_ϕ are two important wing load indicators. Their values would deviate from the trim condition during aircraft maneuvers, under the excitations of atmospheric disturbances, as well as under flap inputs. In a trimmed flight, when an aircraft encounters disturbances, a reasonable control objective is to maintain F_w and M_ϕ at their trimmed values. However, this objective is not applicable during aircraft maneuvers for two reasons: 1) in view of Eq. (9), the wing-root shear force F_w, which is strongly coupled with the total lift on a half-wing, is the main medium for changing flight path angle γ; 2) as discussed in Sec. III.C, the difference between the left and right wing-root bending moments $M_{\phi,\text{diff}}$ is the main medium for aircraft roll control.

Based on these discussions, it is essential to identify the loads that are *necessary* to achieve the commanded maneuvers, while reducing any *excessive* load induced by either maneuvers or external disturbances. A novel reference generator is designed to fulfill this goal. The designed references for the left and right wing-root shear forces are

$$F^{\text{ref}}_{w,r} = F^{\text{ref}}_{w,l} = F^{\text{trim}}_{w} + G_{F_w}(s)(\alpha^{\text{ref}} - \alpha^{\text{trim}}) \tag{20}$$

In Eq. (20), α^{ref} is the angle-of-attack reference designed in Sec. III.B. The term $G_{F_w}(s)$ represents an estimated mapping from α to the open-loop shear force response of a half wing. In this paper, $G_{F_w}(s)$ is designed as a low-pass filer, where s represents the Laplace variable. The zero-frequency gain of $G_{F_w}(s)$ equals $q_\infty S_w C_{L\alpha_w}/2$, where S_w is the wing area and $C_{L\alpha_w}$ is the lift-slope of the wing. The dynamics of $G_{F_w}(s)$ are caused by the time-dependent circulatory effects. Therefore, the time constant of $G_{F_w}(s)$ can be either calculated using Theodorsen's theory [32] or identified online (the output F_w can be measured by strain gauges). If $\alpha^{\text{ref}} = \alpha^{\text{trim}}$, the shear force references are identical to their trim values, and any variations caused by disturbances or maneuvers (such as the lift drop during a sharp-roll) will be automatically counteracted by flaps. Furthermore, define $M_{\phi,a} = M^{\text{trim}}_{\phi,r} - M^{\text{ref}}_{\phi,\text{diff}}/2$ and $M_{\phi,b} = M^{\text{trim}}_{\phi,l} + M^{\text{ref}}_{\phi,\text{diff}}/2$, then the left and right wing-root bending moment references are designed as follows:

$$M^{\text{ref}}_{\phi,r} = \begin{cases} M_{\phi,a}, & \text{if } \max\{M_{\phi,a}, M_{\phi,b}\} \le \overline{M}^{\text{ref}}_{\phi} \\ \overline{M}^{\text{ref}}_{\phi}, & \text{if } M_{\phi,b} \le \overline{M}^{\text{ref}}_{\phi} < M_{\phi,a} \\ \overline{M}^{\text{ref}}_{\phi} - M^{\text{ref}}_{\phi,\text{diff}}, & \text{if } M_{\phi,a} \le \overline{M}^{\text{ref}}_{\phi} < M_{\phi,b} \end{cases} \tag{21}$$

$$M^{\text{ref}}_{\phi,l} = \begin{cases} M_{\phi,b}, & \text{if } \max\{M_{\phi,a}, M_{\phi,b}\} \le \overline{M}^{\text{ref}}_{\phi} \\ M^{\text{ref}}_{\phi,\text{diff}} + \overline{M}^{\text{ref}}_{\phi}, & \text{if } M_{\phi,b} \le \overline{M}^{\text{ref}}_{\phi} < M_{\phi,a} \\ \overline{M}^{\text{ref}}_{\phi}, & \text{if } M_{\phi,a} \le \overline{M}^{\text{ref}}_{\phi} < M_{\phi,b} \end{cases} \tag{22}$$

in which $M^{\text{ref}}_{\phi,\text{diff}}$ has been designed in Sec. III.C, which is the core for achieving the designed roll angle tracking performance. The term $\overline{M}^{\text{ref}}_{\phi}$ is the upper limit on the reference for wing-root bending moment M_ϕ, which can be designed *much smaller* than the real *physical* limit $\max(M_\phi)$, i.e., $M^{\text{trim}}_{\phi,l} = M^{\text{trim}}_{\phi,r} < \overline{M}^{\text{ref}}_{\phi} < \max(M_\phi)$. This can ensure a safety margin from $\max(M_\phi)$ and is also able to constrain the variations of M_ϕ for extending structural fatigue life. The condition $\overline{M}^{\text{ref}}_{\phi} < \min\{M_{\phi,a}, M_{\phi,b}\}$ is not included in Eqs. (21) and (22) because it leads to $\overline{M}^{\text{ref}}_{\phi} < M^{\text{trim}}_{\phi,r}$.

As formulated in Eqs. (21) and (22), to achieve a moderate roll maneuver, the left and right wings take the same responsibility. However, once one of the wing-root bending moments reaches $\overline{M}^{\text{ref}}_{\phi}$ (e.g., during a sharp-roll maneuver), the exceeded command will be automatically allocated to the other half wing. In this way, not only the wing loads are constrained, but $M^{\text{ref}}_{\phi,\text{diff}}$ is achieved for roll command tracking as well.

Remark 4: The wing-root shear force and bending moment references use very little model information and are easy to be implemented in real time. More importantly, by exploiting the control redundancy, the load alleviation is achieved without degrading the command tracking performance.

After the references $F^{\text{ref}}_{w,r}, F^{\text{ref}}_{w,l}, M^{\text{ref}}_{\phi,r}, M^{\text{ref}}_{\phi,l}$ are derived, a controller should be designed to track these references. Taking the right wing as an example, only two independent control variables are needed for tracking $F^{\text{ref}}_{w,r}$ and $M^{\text{ref}}_{\phi,r}$. Because there are seven flaps on each wing, the remaining control space can be used for flutter suppression, aeroelastic damping enhancement, control energy reduction, etc. Choose the controlled output as $\boldsymbol{y}_w = [F_{w,r}, M_{\phi,r}]^\intercal$. This $\boldsymbol{y}_w$ can also be augmented by the loads at several other critical locations. The right wing dynamics given by Eqs. (3) and (4) are represented as

$$\begin{aligned} \dot{\boldsymbol{x}}_e &= \boldsymbol{A}\boldsymbol{x}_e + \boldsymbol{B}_u\boldsymbol{u}_w + \boldsymbol{B}_g\boldsymbol{\alpha}_g + \boldsymbol{B}_{\text{grav}} + \boldsymbol{B}_r\boldsymbol{\alpha}_{qs,r} + \boldsymbol{B}_{\text{acc}}, \\ \boldsymbol{y}_w &= \boldsymbol{C}\boldsymbol{x}_e + \boldsymbol{D}_u\boldsymbol{u}_w + \boldsymbol{D}_{\text{grav}} + \boldsymbol{D}_r\boldsymbol{\alpha}_{qs,r} + \boldsymbol{D}_{\text{acc}} \end{aligned} \tag{23}$$

Further design an augmented state vector $\boldsymbol{X} = \left[\boldsymbol{x}_e^\intercal, \int \boldsymbol{e}_y^\intercal\right]^\intercal$, where $\boldsymbol{e}_y = \boldsymbol{y}_w - \boldsymbol{y}^{\text{ref}}_w$ is for load command tracking, then the augmented system dynamics are

$$\begin{aligned} \begin{bmatrix} \dot{\boldsymbol{x}}_e \\ \boldsymbol{e}_y \end{bmatrix} &= \begin{bmatrix} \boldsymbol{A} & \boldsymbol{0} \\ \boldsymbol{C} & \boldsymbol{0} \end{bmatrix}\begin{bmatrix} \boldsymbol{x}_e \\ \int \boldsymbol{e}_y \end{bmatrix} + \begin{bmatrix} \boldsymbol{B}_u \\ \boldsymbol{D}_u \end{bmatrix}\boldsymbol{u}_w + \begin{bmatrix} \boldsymbol{B}_r \\ \boldsymbol{D}_r \end{bmatrix}\boldsymbol{\alpha}_{qs,r} \\ &\quad + \begin{bmatrix} \boldsymbol{B}_{\text{g}} \\ \boldsymbol{0} \end{bmatrix}\boldsymbol{\alpha}_g + \begin{bmatrix} \boldsymbol{B}_{\text{grav}} \\ \boldsymbol{D}_{\text{grav}} \end{bmatrix} + \begin{bmatrix} \boldsymbol{B}_{\text{acc}} \\ \boldsymbol{D}_{\text{acc}} \end{bmatrix} + \begin{bmatrix} \boldsymbol{0} \\ -\boldsymbol{y}^{\text{ref}}_w \end{bmatrix} \end{aligned} \tag{24}$$

To evaluate the control robustness, the disturbance input $\boldsymbol{\alpha}_g$ and the inertial input vector $[\boldsymbol{B}^\intercal_{\text{acc}}, \boldsymbol{D}^\intercal_{\text{acc}}]^\intercal$ are eliminated from the model used for control design. The control performance can be further enhanced if upstream knowledge of $\boldsymbol{\alpha}_g$ is available (from LIDAR or a gust estimator). The local quasi-steady angle of attack induced by rigid-body translational and rotational motion $\boldsymbol{\alpha}_{qs,r}$ is treated as a known input in wing control design. In addition, the gravitational forces are also treated as known inputs in wing control design. Formulate a cost function as $J = \lim_{t_f\to\infty}(1/2)\int_0^{t_f}[\boldsymbol{X}^\intercal\boldsymbol{Q}\boldsymbol{X} + \boldsymbol{u}_w^\intercal\boldsymbol{R}\boldsymbol{u}_w]\,\text{d}t$, where $\boldsymbol{Q}$ and $\boldsymbol{R}$ are positive definite diagonal matrices. Denote the augmented system dynamic matrix as $\boldsymbol{A}_{\text{aug}}$, and denote $\boldsymbol{B}_{\text{aug}} = [\boldsymbol{B}^\intercal_u, \boldsymbol{D}^\intercal_u]^\intercal$, then the infinite time-horizon optimal control is designed as

$$\begin{aligned} \boldsymbol{u}_w = \boldsymbol{K}_X\boldsymbol{X} + \boldsymbol{K}_r\Big(&\begin{bmatrix} \boldsymbol{B}_r^\intercal & \boldsymbol{D}_r^\intercal \end{bmatrix}^\intercal\boldsymbol{\alpha}_{qs,r} + \begin{bmatrix} \boldsymbol{B}^\intercal_{\text{grav}} & \boldsymbol{D}^\intercal_{\text{grav}} \end{bmatrix}^\intercal \\ &+ \begin{bmatrix} \boldsymbol{0}^\intercal & -(\boldsymbol{y}^{\text{ref}}_w)^\intercal \end{bmatrix}^\intercal\Big) \end{aligned} \tag{25}$$

where $\boldsymbol{K}_X = -\boldsymbol{R}^{-1}\boldsymbol{B}^\intercal_{\text{aug}}\boldsymbol{W}$ and $\boldsymbol{K}_r = -\boldsymbol{R}^{-1}\boldsymbol{B}^\intercal_{\text{aug}}(\boldsymbol{W}\boldsymbol{B}_{\text{aug}}\boldsymbol{R}^{-1}\boldsymbol{B}^\intercal_{\text{aug}} - \boldsymbol{A}^\intercal_{\text{aug}})^{-1}\boldsymbol{W}$. The solution of the associated Riccati equation is denoted as $\boldsymbol{W}$. The designed control input can achieve the following goals:

1) stabilize the aeroelastic system (flutter suppression); 2) track load commands; 3) minimize control energy. The states needed for feedback control are observed by a Kalman filter [18]. The overall control architecture is illustrated in Fig. 2.

IV. Simulation Results and Discussion

In this section, the effectiveness of the proposed control architecture will be evaluated. The flexible aircraft is shown in Fig. 3, whose aspect ratio equals 26.67 and total mass equals 227 kg. Its moment of inertia in trim condition is $I_{xx} = 493.8\ \text{kg}\cdot\text{m}^2$, $I_{yy} = 726.7\ \text{kg}\cdot\text{m}^2$, $I_{zz} = 1170.5\ \text{kg}\cdot\text{m}^2$, and $I_{xz} = -34.0\ \text{kg}\cdot\text{m}^2$. During maneuvers, these inertia will change with structural deformations. For each one of the wing beams, the number of structural elements is $n_s = 7$, whereas the number of aerodynamic strips is $n_a = 14$. The nearest neighbor method is applied for calculating the interpolation matrices $\boldsymbol{H}_{as}$ and $\boldsymbol{H}_{sa}$ in Eq. (3). The actuator dynamics are modeled as $H(s) = 1/(\tau s + 1)$. For elevator and rudder $\tau = 0.02$ s, whereas τ equals 0.2 s for throttle. There are 14 wing flaps connected to the main wing structure via rotational springs with ± 30 deg of deflection limits. The simulation sampling frequency is 20,000 Hz, but the control frequency is much lower: for the attitude and wing control it is 100 Hz, whereas 50 Hz is used by the position and flight path control. As verified by CS-25 aircraft flight tests, 100 Hz is a reasonable choice for the aircraft attitude incremental control [13].

The selection process and specific settings of control parameters are presented as follows. In the position control loop, $K_Y = 1$ and $K_Z = 1$, which are chosen based on the desired exponential convergence rates. In the flight path angle control loop, $K_\sigma = 3$, which is for achieving the desirable exponential convergence rate for the γ dynamics. The gain selection procedure for ν_s has been discussed in Sec. III.B. The proportion gain K_χ is chosen to be equal to K_σ for achieving the same desired closed-loop dynamics for the flight path and the kinematic azimuth angles. Also, K_σ and K_χ are chosen to be higher than K_Y and K_Z as the inner-loop dynamics are faster. In the attitude control loop, $\boldsymbol{K}_1 = \text{diag}([5,5,5])$, $\boldsymbol{K}_2 = \text{diag}([8,8,8])$, $K_{s,i} = 2, \gamma_{s,i} = 0.7$, and $\forall\ i = 1,2,3$. Amplifying $K_{s,i}$ and decreasing $\gamma_{s,i}$ can enhance the tracking accuracy, but more oscillations may happen in the control commands. Finally, in the optimal multi-objective wing control loop, the $\boldsymbol{Q}$ and $\boldsymbol{R}$ matrices are selected based on the weights on states and control. Specifically, $\boldsymbol{R}$ is chosen as an identity matrix. The weighting matrix $\boldsymbol{Q}$ is diagonal, whose elements associated with $\boldsymbol{x}_e$ are chosen to be 1, whereas the other elements associated with $\int \boldsymbol{e}_y$ are chosen to be 50 for structural load alleviation.

A. Trim and Model Analysis

The free-flying flexible aircraft is trimmed in a steady-level flight condition with $H = 1000$ m and $V = 35$ m/s. The trim solutions are $\alpha^* = 3.626°$, $\delta_e^* = -0.1337°$, and $F_E^* = 101.5$ N. An eigenvalue comparison is shown in Fig. 4, from which it can be seen that most of the flexible aircraft poles appear in the high-frequency range and are in good agreement with those of the clamped wing. In the low-frequency range, a new periodic mode with natural frequency 14.38 rad/s and damping ratio 0.21 emerges. The corresponding eigenvectors indicate that this mode is dominated by the couplings between wing bending and rigid-body roll rate. The fourth subplot shows that because of the couplings, the flexible aircraft short-period damping ratio is only 0.46, which is almost halved as compared with its rigid counterpart (0.84). Moreover, the couplings also make the aperiodic mode move toward the unstable region.

The rigid-body and structural couplings are exposed in the above analyses, which underline the necessity of a multi-objective integrated controller. From Fig. 4, the phugoid mode should be stabilized. Moreover, the damping properties of the short-period, Dutch roll, and the new aeroelastic-lateral coupling modes need to be enhanced. Furthermore, the controller should simultaneously fulfill the trajectory tracking commands and the load alleviation requirements. The effectiveness of the proposed control architecture will be shown in the following subsections.

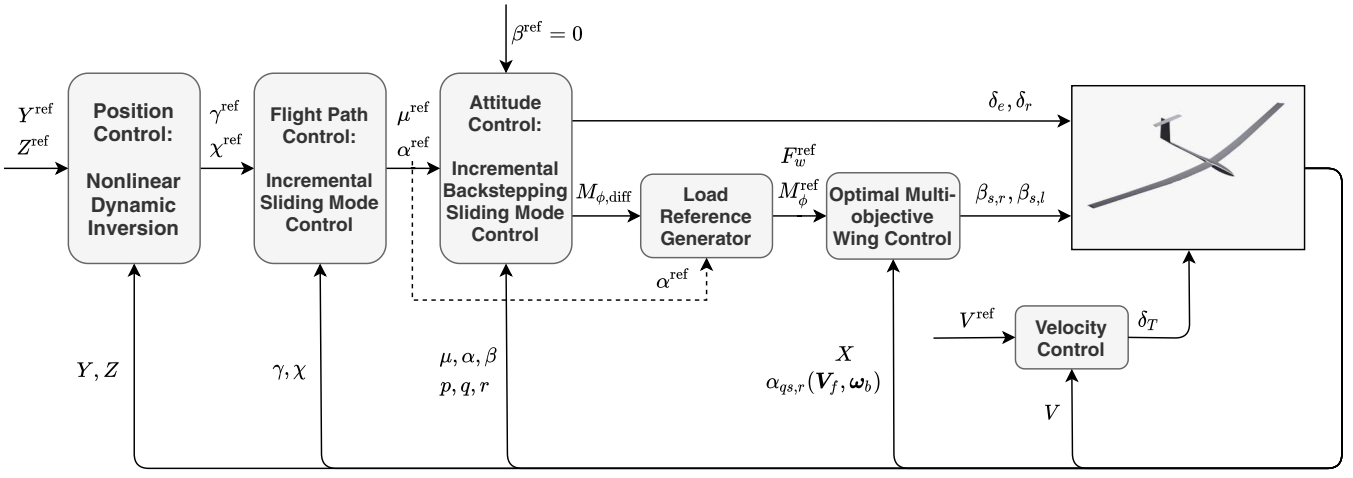

Fig. 2 An illustration of the proposed nonlinear control architecture.

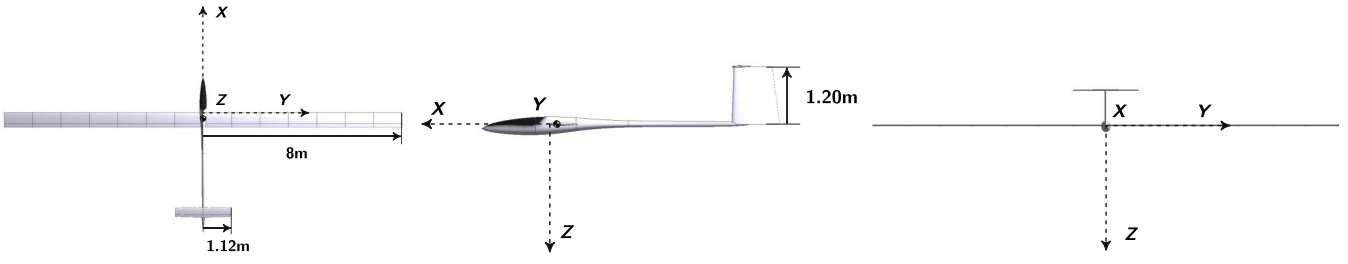

a) Top view (x, y) **b) Side view (x, z)** **c) Back view (y, z)**

Fig. 3 Top, side, and back views of the flexible aircraft.

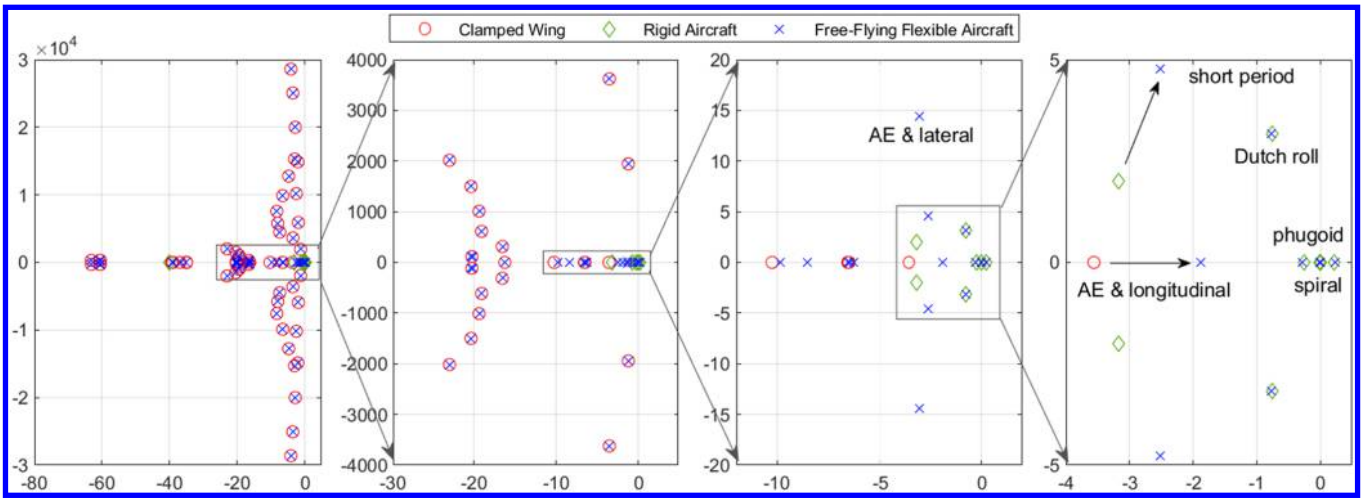

Fig. 4 Eigenvalues of the aeroelastic clamped wing, the rigid aircraft, and the free-flying flexible aircraft.

B. Maneuver Load Alleviation

Four maneuver circumstances will be considered: sudden pull-up, sharp roll, flight path tracking, and 3D aircraft position tracking. The controller aims at minimizing the tracking errors while alleviating the maneuver loads.

1. *Load Alleviation in a Pull-Up Maneuver*

In this simulation case, the aircraft is commanded to track an α profile; the kinematic bank angle and the side-slip angle are commanded to maintain zero. As illustrated in the first subplot of Fig. 5, two smoothly combined sigmoid functions $f_1 = 1/(1 + e^{-8(t-1)})$ and $f_2 = -1/(1 + e^{-8(t-3)})$ are used to compose the command. Because this maneuver is symmetrical, only the right wing responses are shown.

Another controller without the MLA function (flap hinge moments equal zero) is designed for comparisons. Figure 5 shows that both controllers can track the given α command, with max $(|\alpha - \alpha^{\text{ref}}|) < 0.14°$. Their wing-root shear force responses are also similar. Nevertheless, the wing-root bending moment is effectively reduced by the MLA function. Recall Eqs. (21) and (22); $M^{\text{ref}}_{\phi,r} = M^{\text{trim}}_{\phi,r}$ in symmetrical maneuvers ($M^{\text{ref}}_{\phi,\text{diff}} = 0$). The usage of MLA reduces $\max(|M_{\phi,r} - M^{\text{trim}}_{\phi,r}|)$ from 4183 to 1.344 N · m (by 99.97%) and reduces $\text{rms}(|M_{\phi,r} - M^{\text{trim}}_{\phi,r}|)$ from 2387 to 0.5827 N · m (by 99.98%). Figure 6a shows that the MLA makes the inner-board flaps ($\beta_{s_i,r}, i = 1, 2, 3$) deflect downward and the out-board flaps ($\beta_{s_i,r}, i = 5, 6, 7$) deflect upward, which shifts the pressure center toward the wing root. More importantly, by exploiting the control redundancy, the α tracking performance is not influenced by the MLA function (Fig. 5).

2. *Load Alleviation in a Sharp-Roll Maneuver*

The aircraft is commanded to roll from 0 to 40 deg within 2 s. The sigmoid function $f_3 = 1/(1 + e^{-6(t-2)})$ is adopted as a smooth realization of the step function. For comparisons, another controller without MLA is designed, which differs from the nominal one in two aspects: 1) the shear force command tracking is deactivated; 2) the right and left wing always share the same responsibility in roll tracking, i.e., $M^{\text{ref}}_{\phi,r} \equiv M^{\text{trim}}_{\phi,r} - M^{\text{ref}}_{\phi,\text{diff}}/2$, $M^{\text{ref}}_{\phi,l} \equiv M^{\text{trim}}_{\phi,l} + M^{\text{ref}}_{\phi,\text{diff}}/2$. To demonstrate the effectiveness of the proposed control architecture, the upper limit on the reference for wing-root bending moment $\overline{M}^{\text{ref}}_{\phi}$ is set at 5000 N · m, which is *much lower* than the real physical limit on M_ϕ.

Figure 7 shows that the kinematic bank angle tracking responses with and without MLA are almost identical, with max $(|\mu - \mu^{\text{ref}}|) < 0.66°$. The second subplot of Fig. 7 shows that without MLA, $F_{w,r}$ and $F_{w,l}$ have large variations because of the $\boldsymbol{\alpha}_{qs,r}$ induced by roll maneuvers. By contrast, the MLA function can compensate for the variations, since $F^{\text{ref}}_{w,r} = F^{\text{ref}}_{w,l} = F^{\text{trim}}_{w}$ when $\alpha^{\text{ref}} = 0$ [Eq. (20)]. When using the MLA function, $\text{rms}(F_{w,r} - F^{\text{ref}}_{w,r})$ is reduced from 63.83 to 6.235 N (by 90.23%). Moreover, as illustrated in the third and fourth subplots, the MLA algorithm successfully complies with the strict limit $\overline{M}^{\text{ref}}_{\phi} = 5000$ N · m. Once one of $M_{\phi,r}$ and $M_{\phi,l}$ reaches $\overline{M}^{\text{ref}}_{\phi}$, the exceeded command is automatically allocated to the other wing without influencing the roll tracking performance. On the contrary, if the MLA algorithm is deactivated, $\max(M_{\phi,r}) = 5634$ N · m and $\max(M_{\phi,l}) = 5578$ N ·m. By actuating the distributed trailing-edge control surfaces, not only the loads are alleviated, but the maximum wing deflection is reduced as well (Fig. 8). In addition, the flap deflection angles remain within the ±30 deg limits (Fig. 8a).

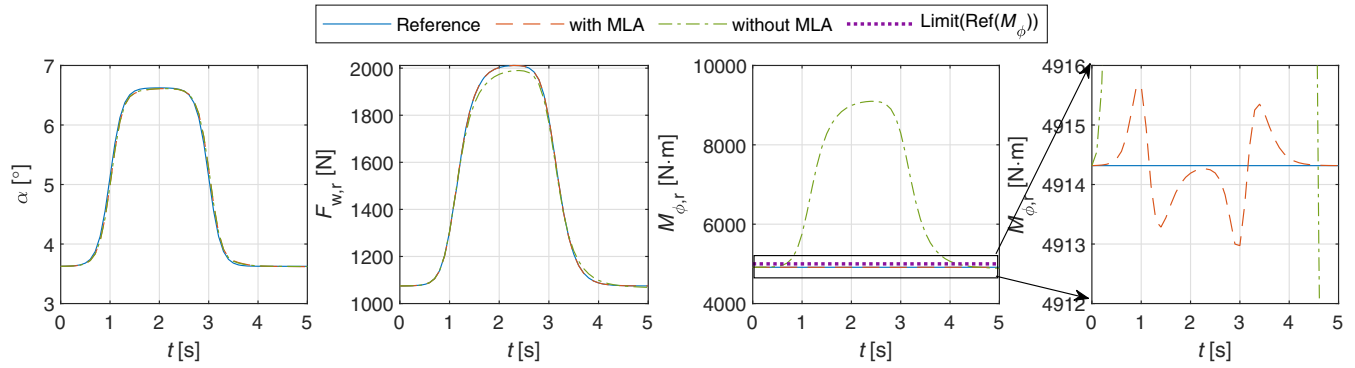

Fig. 5 The tracking performance of α and the responses of wing-root shear force and bending moment.

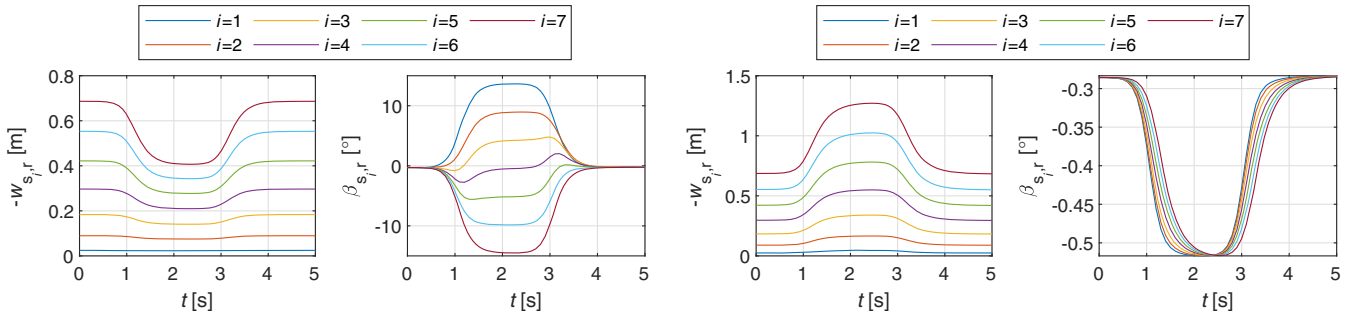

a) With MLA b) Without MLA

Fig. 6 Responses of the right wing displacements $-w_{s_i,r}$ and flap angles $\beta_{s_i,r}$ (i is the structural node index).

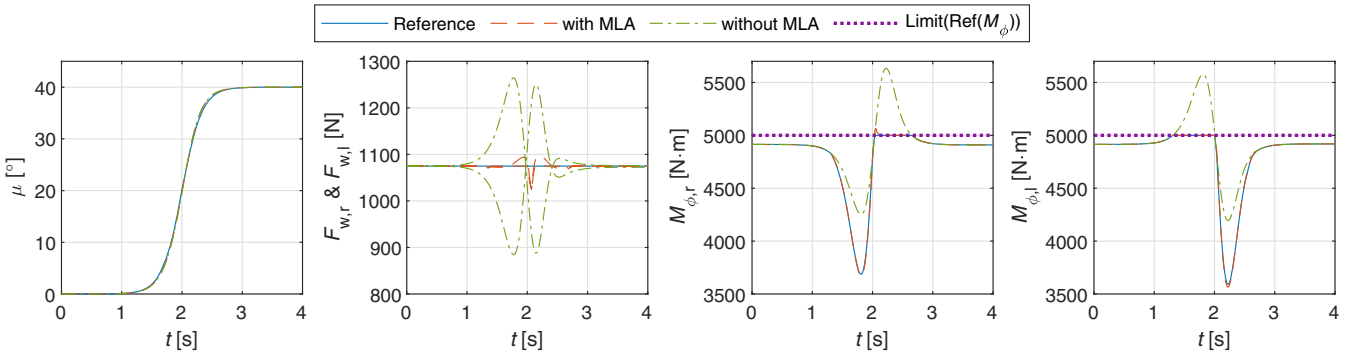

Fig. 7 Responses of the kinematic bank angle, wing-root shear force, and bending moment.

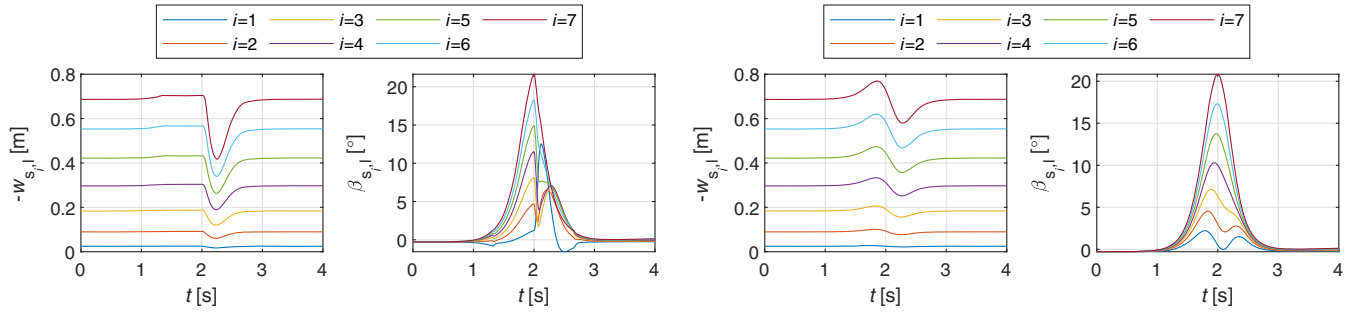

a) With MLA b) Without MLA

Fig. 8 Responses of the left wing displacements $-w_{s,l_i}$ and flap angles β_{s,l_i} (i is the structural node index).

3. Flight Path Control with Maneuver Load Alleviation

The aircraft is commanded to follow a spiral trajectory shown in Fig. 9, which is realized by giving a step command to the flight path angle γ, and a ramp command to the kinematic azimuth angle χ. The upper limit on the reference for wing-root bending moment is $\overline{M}_{\phi}^{\text{ref}} = 5000\ \text{N} \cdot \text{m}$. Figure 9 shows that the proposed controller can

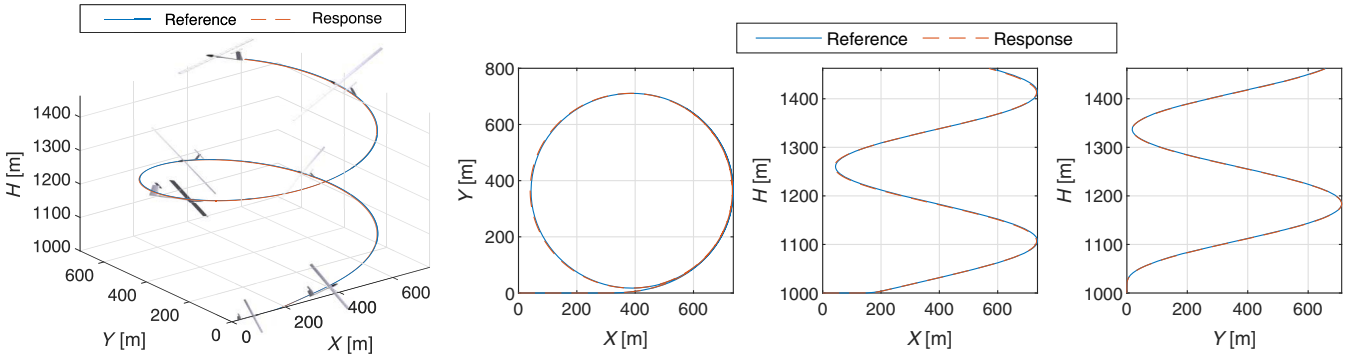

a) 3D spiral trajectory tracking b) Three views of the 3D spiral tracking

Fig. 9 Aircraft 3D spiral trajectory tracking performance.

make the flexible aircraft track the given command, with $\max(|X - X^{\text{ref}}|) < 3.10$ m, $\max(|Y - Y^{\text{ref}}|) < 0.11$ m, and $\max(|H - H^{\text{ref}}|) < 0.42$ m.

Figure 10 shows that the flight path angle increases from 0 to 8 deg within 3.5 s, with maximum tracking error equaling 0.19°. The ramp command (slope 5.73°/s) for the kinematic azimuth angle χ is tracked with $\max(|e_\chi|) = 0.026°$. The aircraft velocity is maintained at the trimmed value using throttle control. The attitude commands given by the flight path control loop are also tracked, with $\max(|e_\mu|) = 0.34°$, $\max(|e_\alpha|) = 0.12°$, and $\max(|e_\beta|) = 0.013°$.

The corresponding load responses are shown in Fig. 11a. When $t \in [0, 8]$ s, only symmetrical states are excited; thus $M_{\phi,r}$ and $M_{\phi,l}$ are maintained at their trimmed values, whereas $F_{w,r}$, $F_{w,l}$ are driven to realize the γ tracking command. In addition, the wing displacements and flap deflections are also symmetrical (Fig. 11b). When $t \in [8, 25]$ s, the aircraft starts entering the spiral. Similar to the responses in the sharp-roll maneuver (Fig. 7), in case one of $M_{\phi,r}$ and $M_{\phi,l}$ reaches $\overline{M}_\phi^{\text{ref}}$, the exceeded load is automatically reallocated via flap deflections (Fig. 11). The elevator (δ_e), rudder (δ_r), and thrust inputs in this spiral maneuver are plotted in Fig. 12.

4. *Position Control with Maneuver Load Alleviation*

A more complex 3D maneuver with strongly coupled longitudinal and lateral motions will be tested in this subsection. Figure 13 shows that the trajectory references are tracked with $\max(|X - X^{\text{ref}}|) < 1.4$ m, $\max(|Y - Y^{\text{ref}}|) < 0.019$ m, and $\max(|H - H^{\text{ref}}|) < 0.023$ m. The rigid-body responses are shown in Fig. 14, where $\max(|e_\gamma|) = 0.0736°$ and $\max(|e_\chi|) = 0.0604°$. The proposed nonlinear controller can decouple dynamics through the control effectiveness inversion. As a result, the pitch, roll, and yaw channels are driven by their own desired tracking error dynamics [Eq. (17)].

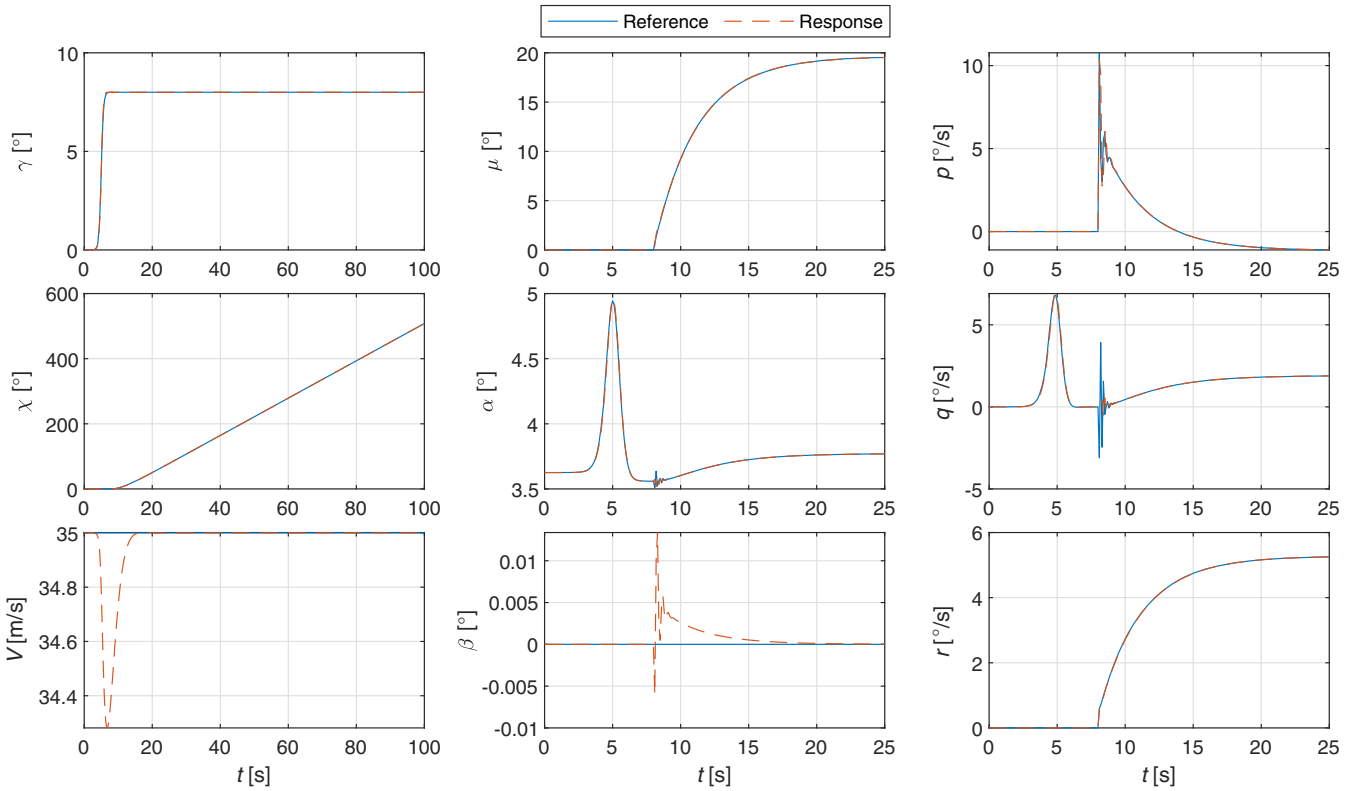

Fig. 10 Responses of flight path angles, attitude angles, and angular rates during a spiral maneuver.

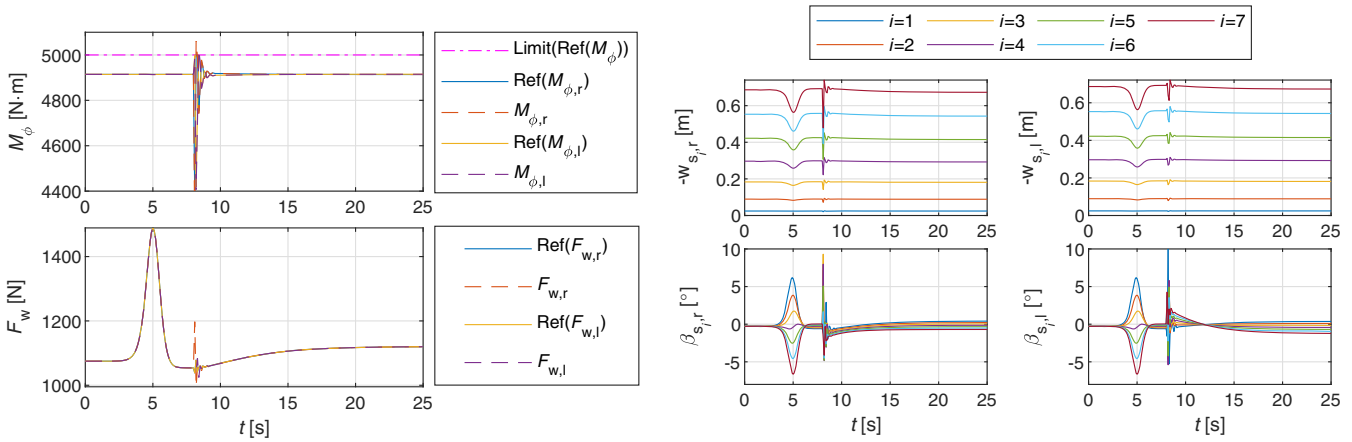

a) Load responses **b) Wing displacements and flap deflections**

Fig. 11 Responses in a 3D spiral trajectory tracking maneuver.

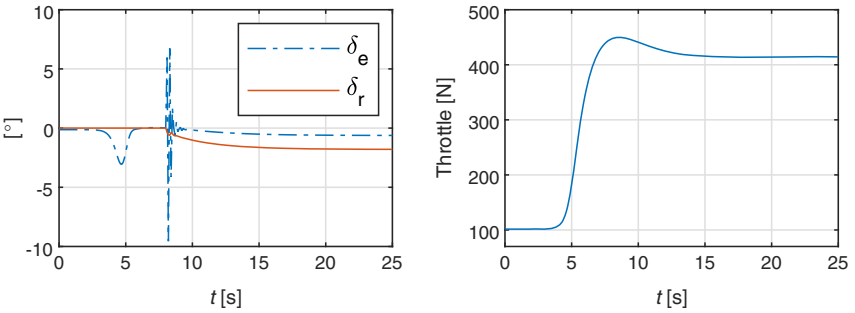

Fig. 12 Inputs of elevator (δ_e), rudder (δ_r), and thrust in an aircraft spiral maneuver.

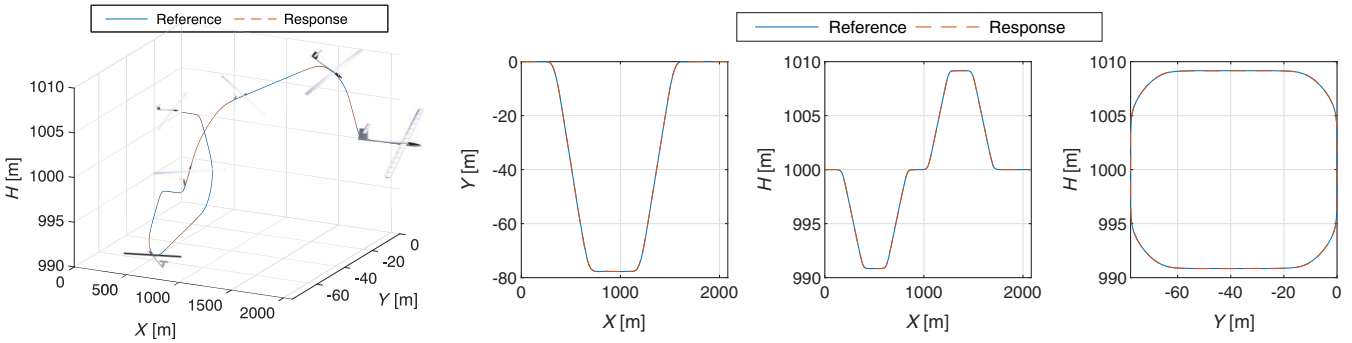

a) 3D position tracking **b) Three views of the 3D position tracking**

Fig. 13 Aircraft 3D position tracking performance.

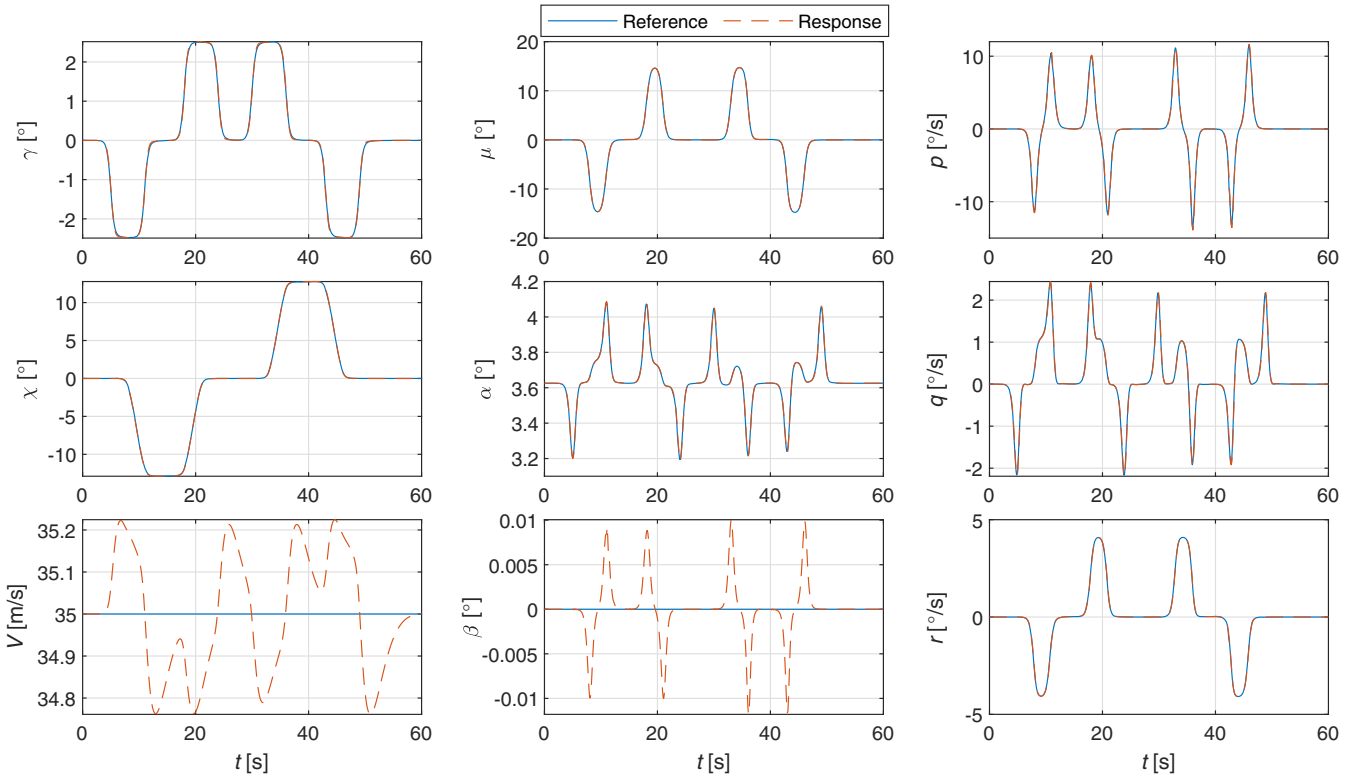

Fig. 14 Responses of flight path angles, attitude angles, and angular rates in an aircraft 3D maneuver.

The load responses are shown in Fig. 15a. The differences between the right and left bending moments are necessary for achieving lateral maneuvers (Sec. III.C). By virtue of the MLA algorithm, $\overline{M}_{\phi}^{\text{ref}}$ is not exceeded. The variations of F_w are needed for flight path angle tracking. The maximum wing-tip displacement equals 0.74 m, which only deviates 0.06 m from its nominal value (Fig. 15b). The flap

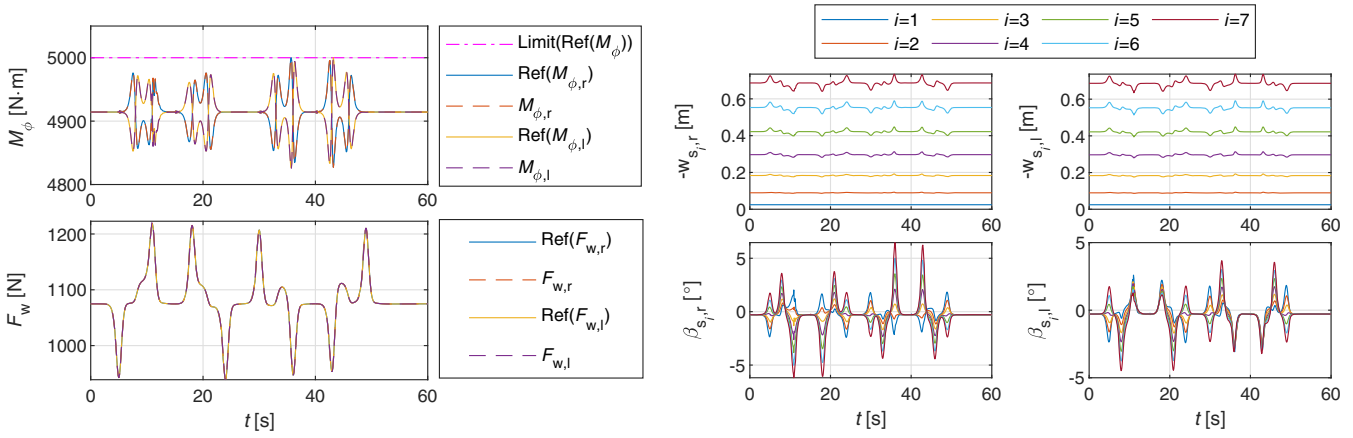

a) Load responses **b) Wing displacements and flap deflections**

Fig. 15 Responses in a 3D position tracking maneuver.

deflections are smooth and are within the ±30 deg limit (Fig. 15b). Figure 16 shows that the elevator (δ_e), rudder (δ_r), and thrust inputs are smooth and are also within their limits.

C. Gust Load Alleviation

This subsection will evaluate the GLA performance of the proposed controller. The 2D spatial von Kármán turbulence model is adopted, which considers the gust penetration effect and spanwise gust variations [18]. The control objective is to maintain the cruise flight, while alleviating the loads induced by turbulence (Fig. 17). The open-loop responses shown in the following figures represent the aircraft with stabilized phugoid mode (via velocity feedback control). Even so, the elevator, rudder, and flap hinge moments are set to zero in the open-loop case.

Using the superscript "∗" to denote the trimmed value, then in Fig. 18a, $\text{rms}(n_z - n_z^*)$ is reduced from 0.439 to 0.0159 g (by 96.38%), $\text{rms}(M_{\phi,r} - M_{\phi,r}^*)$ is alleviated from 2057 to 16.45 N · m (by 99.20%), and $\text{rms}(F_{w,r} - F_{w,r}^*)$ is diminished by 92.43%. For the high-aspect-ratio aircraft considered in this paper, the turbulence field intensively influences the roll channel (Fig. 18b), where $\text{rms}(p)$ equals 23.5°/s in the open-loop case, which is reduced by 99.65% using the proposed controller. Moreover, $\text{rms}(q)$ and $\text{rms}(r)$ are diminished by 97.48 and 91.57%, respectively.

Figure 19 shows that the structural vibrations are damped by the proposed controller. The maximum deviation of the wing tip is reduced from 1.5 to 0.81 m (by 46.00%). When the control loop is closed, the flaps deflect against the turbulence profile and also modify the spanwise lift distributions. The deflection angles are within ±30 deg (Fig. 19b). Figure 20 shows that, in the closed-loop case, elevator (δ_e) and rudder (δ_r) are actively deflected for suppressing the rigid-body motions in this severe turbulence field.

D. Simultaneous Gust and Maneuver Load Alleviation

In this subsection, the aircraft is driven to track a 3D trajectory in a 2D light von Kármán turbulence field ($L_g = 762$ m, $\sigma = 2.2$ m/s).

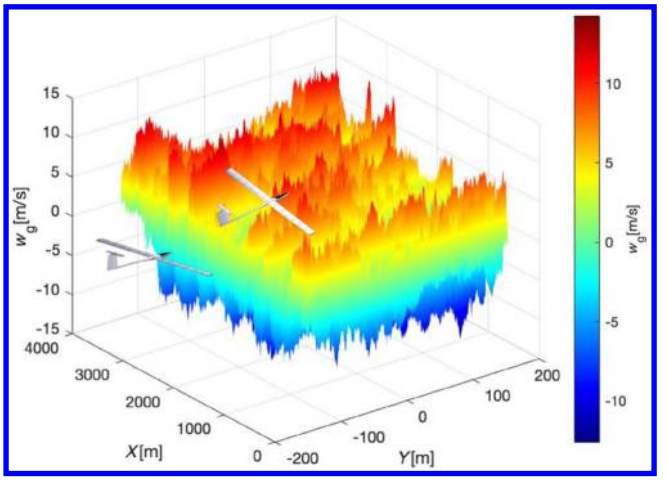

Fig. 17 A 2D severe von Kármán turbulence field ($L_g = 762$ m, $\sigma = 6$ m/s).

Figure 21 illustrates that the open-loop case deviates from the references and eventually crashes. By contrast, the proposed controller still drives the aircraft along the trajectory in spite of disturbances, with $\max(|X - X^{\text{ref}}|) < 1.4$ m, $\max(|Y - Y^{\text{ref}}|) < 0.020$ m, and $\max(|H - H^{\text{ref}}|) < 0.023$ m.

Figure 22 shows that, in the open-loop case, the accumulated roll angle tracking error leads to a severe lift drop, which further makes the aircraft dive toward the ground. On the contrary, by virtue of the control redundancy, the proposed controller can simultaneously make the aircraft reject disturbances and track commands with small errors ($\max(|e_\gamma|) = 0.080°$, $\max(|e_\chi|) = 0.059°$, $\max(|e_\mu|) = 0.10°$, $\max(|e_\alpha|) = 0.039°$, and $\max(|e_\beta|) = 0.012°$).

The open-loop load responses present large variations, and the load factor gradually deviates from its trimmed value (Fig. 23a).

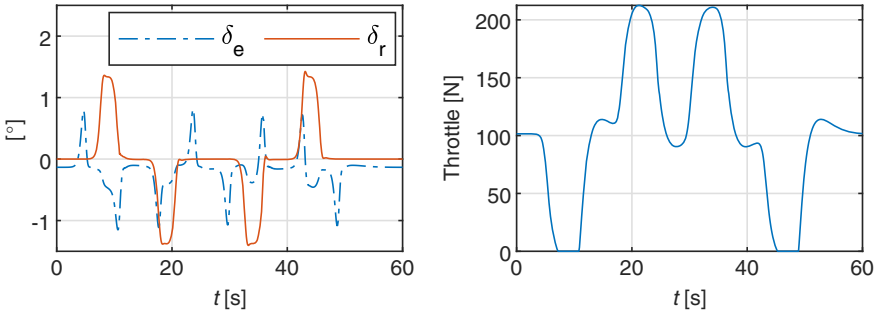

Fig. 16 Inputs of elevator (δ_e), rudder (δ_r), and thrust in a 3D position tracking maneuver.

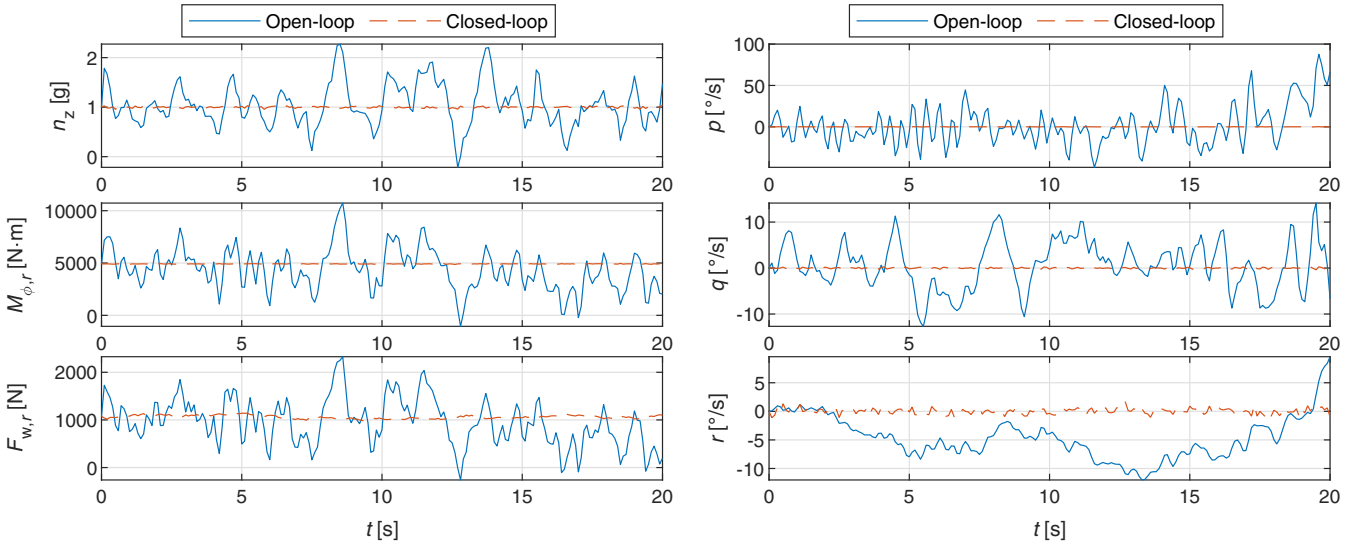

Fig. 18 Aircraft responses in a 2D von Kármán turbulence field.

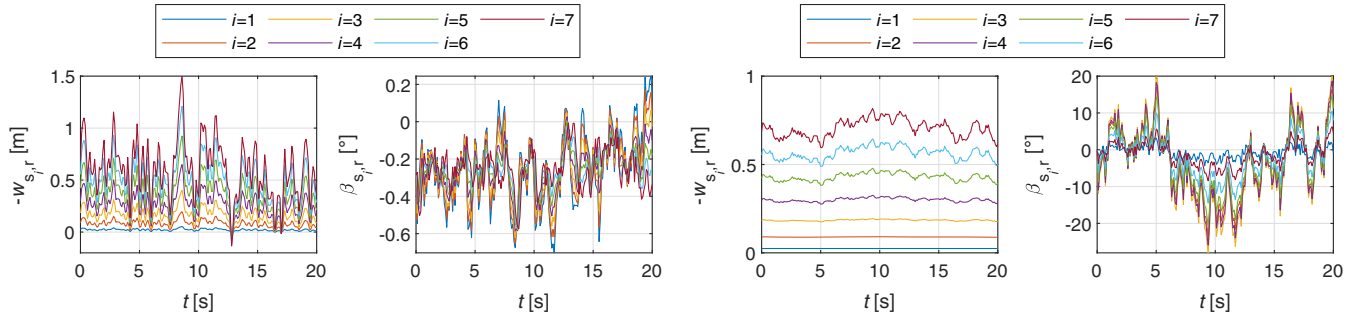

a) Open-loop responses **b) Closed-loop responses**

Fig. 19 The right wing displacements ($-w_{s_i,r}$) and flap deflections ($\beta_{s_i,r}$) in a 2D von Kármán turbulence field.

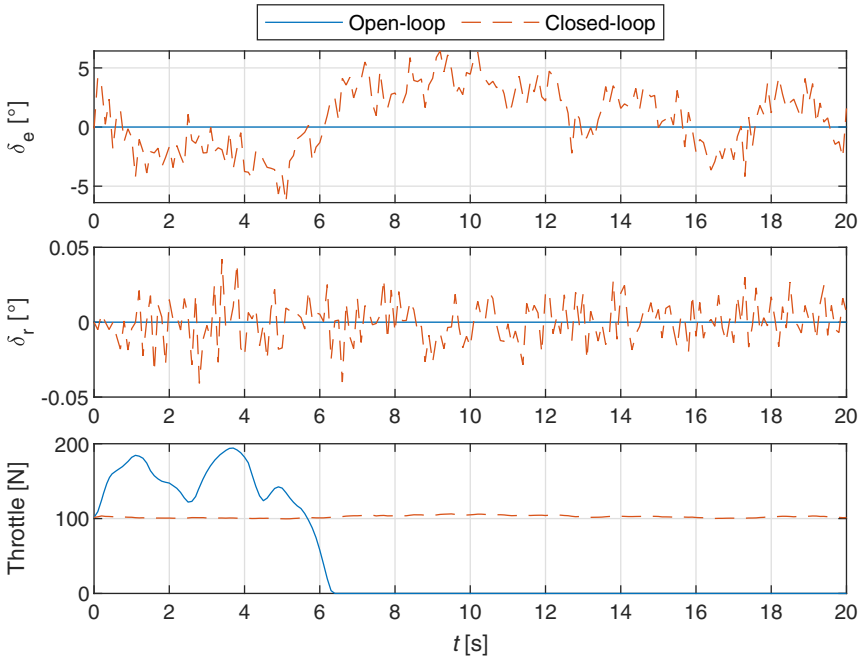

Fig. 20 Inputs of elevator, rudder, and thrust in a 2D severe von Kármán turbulence field.

Conversely, the controller neutralizes the excessive loads (no matter caused by maneuvers or turbulence) and achieves max $(|n_z - n_z^*|) = 0.159$ g, $\max(|M_{\phi,r} - M_{\phi,r}^{\text{ref}}|) = 51.2$ N · m, and max $(F_{w,r} - |F_{w,r}^{\text{ref}}|) = 17.9$ N. Elevator and rudder are used to simultaneously achieve command tracking and load alleviation (Fig. 23b). The throttle control maintains the velocity within ± 0.5 m/s (Fig. 22).

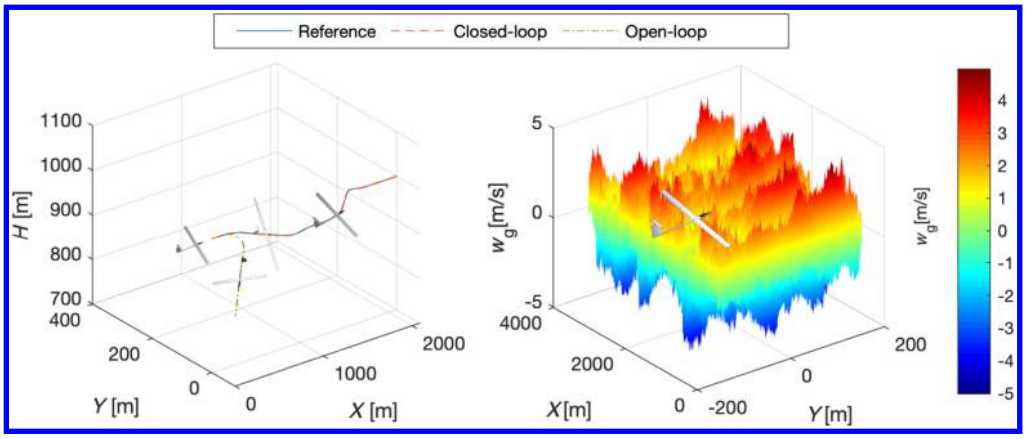

Fig. 21 Three-dimensional trajectory tracking responses in a 2D light von Kármán turbulence field ($L_g = 762$ m, $\sigma = 2.2$ m/s).

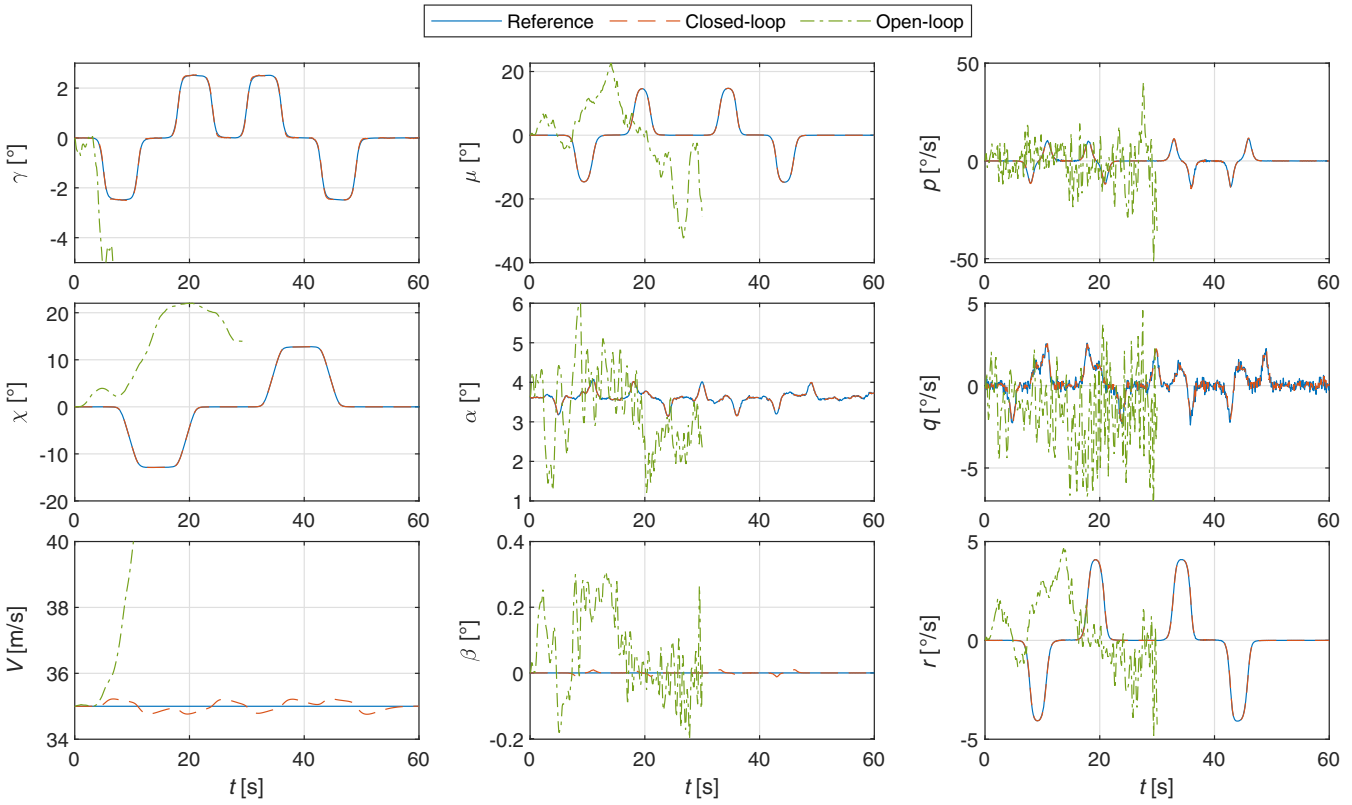

Fig. 22 Responses of flight path angles, attitude angles, and angular rates in a 3D maneuver with turbulence.

However, in the open-loop case, the aircraft starts to dive and the throttle is saturated at its lower limit after $t = 4.8$ s, which is unable to prevent the velocity from amplifying (Fig. 23b).

Figure 24 shows that the wing has severe vibrations in the open-loop case and is damped using the proposed controller, which actively drives the flaps to alleviate loads. The time responses of the spanwise load distributions are shown in Fig. 25. It can be observed that the spanwise shear force $F_{w,r}$, bending moment $M_{\phi,r}$, and torsion moment $M_{\theta,r}$ are all monotonically decreasing from the root to the tip. The time responses of the spanwise displacement fields are illustrated in Fig. 26. Because the bending and torsion shape functions of the beam have $\mathcal{C}^1$ and $\mathcal{C}^0$ continuities, respectively, the vertical displacement $w_{s,r}$, the torsional angle $\theta_{s,r}$, and the first-order partial derivative of $-w_{s,r}$ with respect to the spanwise location x_w are all continuous along the beam throughout the entire time history. In brief, there are three main elements contributing to the strong robustness of the proposed control architecture: 1) the sensor-based nature of the incremental control, 2) the robustness of sliding mode control and observer, and 3) the structural damping enhancement by the optimal wing control.

V. Conclusions

In this paper, a nonlinear control architecture for flexible aircraft trajectory tracking and load alleviation is proposed. To begin with, the free-flying flexible aircraft dynamics are derived, which capture both the inertial and aerodynamic couplings between the rigid-body and structural degrees of freedom. The dynamic model is derived in a modular approach, which provides a convenient way to make an existing clamped-wing aeroservoelastic model free-flying.

Based on the flexible aircraft model, a four-loop cascaded control architecture is proposed. The position control loop is designed using NDI, which provides references to the flight path control loop. The flight path control loop adopts the incremental sliding mode control

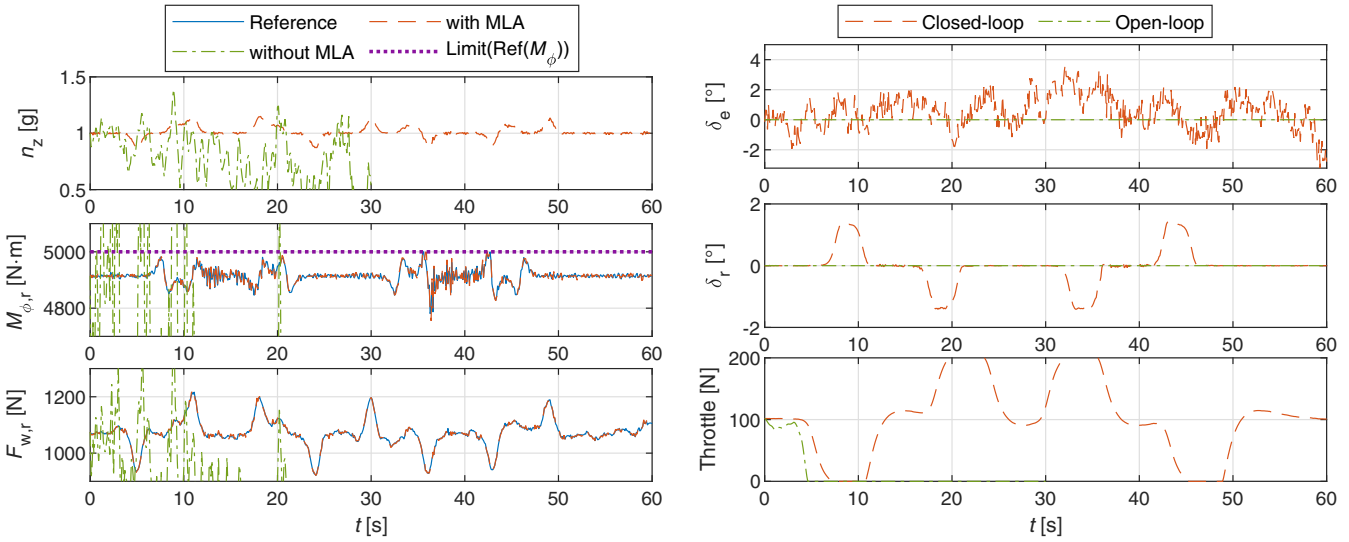

a) Load responses b) Inputs of elevator, rudder, and thrust

Fig. 23 Three-dimensional trajectory tracking under spatial von Kármán turbulence excitations.

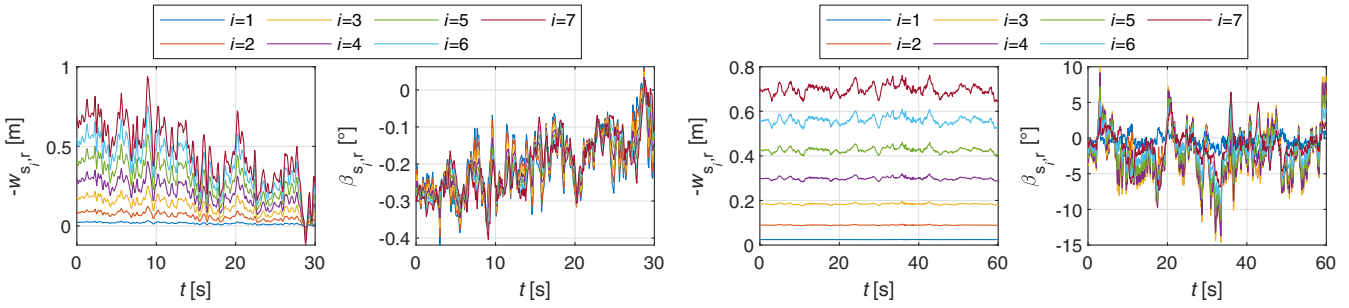

a) Open-loop responses b) Closed-loop responses

Fig. 24 The wing displacements and flap deflections during a trajectory tracking task in a turbulence filed.

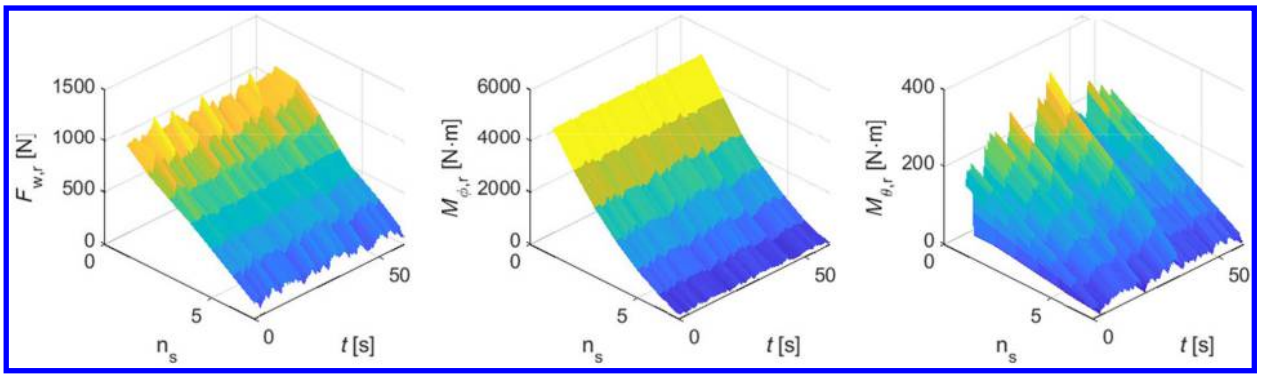

Fig. 25 Time responses of the right wing spanwise load distributions.

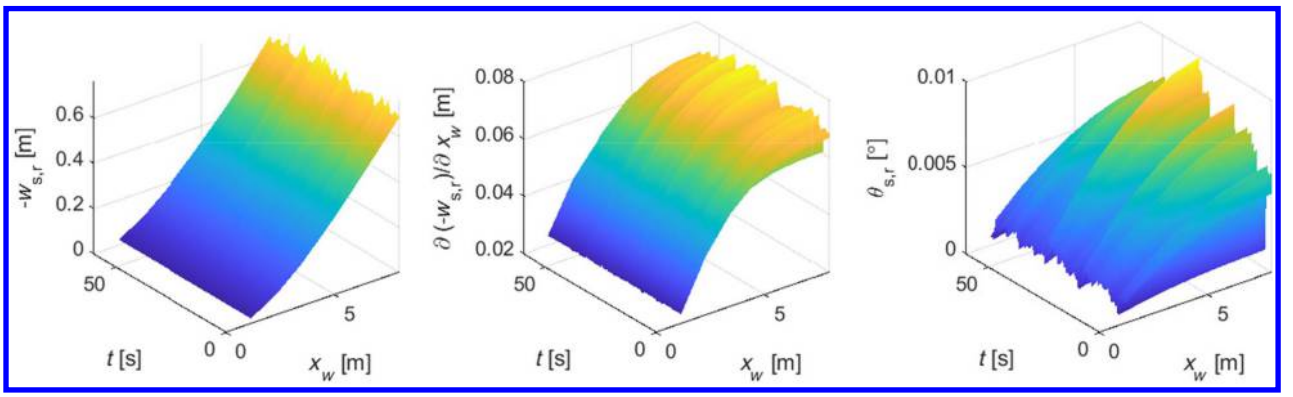

Fig. 26 Time responses of the right wing spanwise displacement fields.

law, whose reduced model dependency and enhanced robustness are demonstrated theoretically. Moreover, the incremental backstepping sliding mode control is used in the attitude control loop. Based on Lyapunov methods, this loop is proven to be stable under disturbance perturbations. Furthermore, a novel load reference generator is proposed, which distinguishes the loads that are necessary to perform maneuvers from the excessive loads. The load references are then tracked by the inner-loop multi-objective wing control. At the same time, the excessive loads (no matter induced by maneuvers or gusts) are naturalized by control surface deflections. Because the proposed control architecture exploits the control redundancy, the load alleviation is achieved without affecting the aircraft command tracking performance.

The effectiveness of the proposed control architecture is validated by numerical simulations. It is demonstrated that the loads during sudden pull-up and sharp roll maneuvers can be alleviated without influencing rigid-body command tracking performance. Moreover, simulations in a severe 2D spatial von Kármán turbulence field verify the robustness of the controller to model uncertainties and external disturbances. Finally, the flexible aircraft is commanded to follow a 3D trajectory in a spatial turbulence field. Simulation results show that both the maneuver and gust loads are effectively alleviated without affecting the trajectory tracking performance. It is recommended to expand the applicability of incremental sliding mode control by designing adaptation laws with thresholds for avoiding singularities and Nussbaum functions for handling unknown control directions.

Appendix A: Inertial Forces

Consider an infinitesimal mass element d m on an arbitrary section A_w of the right wing. When the wing is undeformed, the distance vector from O_w to d m expressed in the right wing reference frame is $\boldsymbol{r}_w = [r_x, r_y, r_z]^\intercal$. Denote the transverse displacement of this wing section as w, and its torsional angle around the $O_w x_w$ axis as θ, then the position vector caused by elastic deformations is

$$\boldsymbol{r}_e = \begin{bmatrix} r_{e,x} \\ r_{e,y} \\ r_{e,z} \end{bmatrix} = \begin{bmatrix} 0 \\ 0 \\ w \end{bmatrix} + \begin{bmatrix} 0 \\ r_y(\cos\theta - 1) \\ r_y \sin\theta \end{bmatrix} \tag{A1}$$

The absolute distance from the inertial frame origin O_I to O_w equals the summation of $\boldsymbol{R}_b$ (defined in the inertial frame) and $\boldsymbol{r}_{wb}$ (defined in the body reference frame). Denote $\boldsymbol{R}_w$ as the absolute distance from O_I to d m, projected on the right wing reference frame, then

$$\boldsymbol{R}_w = \boldsymbol{C}_{WB}\boldsymbol{C}_{BI}\boldsymbol{R}_b + \boldsymbol{C}_{WB}\boldsymbol{r}_{wb} + \boldsymbol{r}_w + \boldsymbol{r}_e \tag{A2}$$

By differentiating the above equation, the absolute velocity of d m expressed in the right wing reference frame equals

$$\begin{aligned} \boldsymbol{V}_w &= \boldsymbol{C}_{WB}\boldsymbol{V}_b + \boldsymbol{C}_{WB}\{\boldsymbol{\omega}_b \times [\boldsymbol{r}_{wb} + \boldsymbol{C}_{WB}^\intercal(\boldsymbol{r}_w + \boldsymbol{r}_e)]\} + \boldsymbol{v}_e \\ &= \boldsymbol{C}_{WB}\boldsymbol{V}_b + \boldsymbol{C}_{WB}\tilde{\boldsymbol{\omega}}_b\boldsymbol{r}_{wb} + \boldsymbol{C}_{WB}\tilde{\boldsymbol{\omega}}_b\boldsymbol{C}_{WB}^\intercal(\boldsymbol{r}_w + \boldsymbol{r}_e) + \boldsymbol{v}_e \end{aligned} \tag{A3}$$

in which $\boldsymbol{V}_b = [V_x, V_y, V_z]^\intercal$ and $\boldsymbol{\omega}_b = [p, q, r]^\intercal$ are the translational and rotational velocities of the body frame, and both of them are expressed in $\mathcal{F}_B$; $\boldsymbol{v}_e$ is the relative deformation velocity of d m, which equals $[\dot{r}_{e,x}, \dot{r}_{e,y}, \dot{r}_{e,z}]^\intercal$; and $\tilde{(\cdot)}$ denotes the skew-symmetric matrix of the vector $(\cdot)$.

Furthermore, differentiate Eq. (A3); the absolute acceleration of d m expressed in the right wing reference frame equals

$$\begin{aligned} \boldsymbol{a}_w &= \boldsymbol{C}_{WB}\boldsymbol{a}_f + \boldsymbol{C}_{WB}\tilde{\boldsymbol{\alpha}}_f\boldsymbol{r}_{wb} + \boldsymbol{C}_{WB}\tilde{\boldsymbol{\alpha}}_f\boldsymbol{C}_{WB}^\intercal(\boldsymbol{r}_w + \boldsymbol{r}_e) \\ &\quad + 2\boldsymbol{C}_{WB}\tilde{\boldsymbol{\omega}}_b\boldsymbol{C}_{WB}^\intercal\boldsymbol{v}_e + \boldsymbol{a}_e + \boldsymbol{C}_{WB}\tilde{\boldsymbol{\omega}}_b\tilde{\boldsymbol{\omega}}_b\boldsymbol{r}_{wb} \\ &\quad + \boldsymbol{C}_{WB}\tilde{\boldsymbol{\omega}}_b\tilde{\boldsymbol{\omega}}_b\boldsymbol{C}_{WB}^\intercal(\boldsymbol{r}_w + \boldsymbol{r}_e) \end{aligned} \tag{A4}$$

where $\boldsymbol{a}_b = [a_x, a_y, a_z]^\intercal$ and $\boldsymbol{\alpha}_b = [\dot{p}, \dot{q}, \dot{r}]^\intercal$ are the translational and rotational accelerations of the body frame, and both of them are expressed in $\mathcal{F}_B$, and $\boldsymbol{a}_e = [\ddot{r}_{e,x}, \ddot{r}_{e,y}, \ddot{r}_{e,z}]^\intercal$ is the relative deformation acceleration of d m. Using Eq. (A4), define $\boldsymbol{a}_I$ as $\boldsymbol{a}_I = \boldsymbol{a}_w - \boldsymbol{a}_e$, then at the wing section A_w, the inertial force per unit length is computed as $\boldsymbol{f}_{\text{acc}} = -\iint_{A_w} \rho \boldsymbol{a}_I \, \mathrm{d}r_y \, \mathrm{d}r_z$, where ρ is the volume density. The inertial moment around $O_w x_w$ per unit length is $\boldsymbol{m}_{\text{acc}} = -\iint_{A_w} \rho [0, r_y, r_z]^\intercal \times \boldsymbol{a}_I \, \mathrm{d}r_y \, \mathrm{d}r_z$.

The distributed inertial forces and moments are integrated to their nearest structural node. Consider the ith structural node with a spanwise location $r_x = x_i$, then the integrated force vector associated with its degrees of freedom is

$$\begin{bmatrix} f_w \\ f_\phi \\ f_\theta \\ f_\beta \end{bmatrix}_{\text{acc},i} = \begin{bmatrix} \int_{x_{i-1}}^{x_i} f_{\text{acc},z} \, \mathrm{d}r_x \\ \int_{x_{i-1}}^{x_i} (x_i - x) f_{\text{acc},z} - m_{\text{acc},x} \, \mathrm{d}r_x \\ \int_{x_{i-1}}^{x_i} m_{\text{acc},y} \, \mathrm{d}r_x \\ 0 \end{bmatrix} \tag{A5}$$

which is valid for $i = 1, \ldots, n_s$. The inertial loads on the structural nodes are collected into a force vector $\boldsymbol{F}_{\text{s,acc}} = [[f_w, f_\phi, f_\theta, f_\beta]_{\text{acc},1}, \ldots, [f_w, f_\phi, f_\theta, f_\beta]_{\text{acc},n_s}]^\intercal \in \mathbb{R}^{4n_s}$.

Appendix B: Supplements for the Flexible Aircraft Flight Dynamics

In Sec. II.B, the flexible aircraft flight dynamics are presented. This appendix will present the explicit expressions for the $\tilde{\boldsymbol{S}}$, $\boldsymbol{J}$, $\boldsymbol{d}_F$, and $\boldsymbol{d}_M$ in Eqs. (5) and (6).

The flexible aircraft model considered in this paper has two flexible components: the left and right wings. The rest components, namely, the fuselage and tail (including vertical and horizontal tails), are assumed to be rigid. Denote the distance vector from O_b to an infinitesimal mass element d m_f on the fuselage as $\boldsymbol{r}_f$, which is expressed in the body-fixed reference frame $\mathcal{F}_B$. Also, define the distance vector from O_b to an infinitesimal mass element d m_t on the tail as $\boldsymbol{r}_t$, which is also expressed in $\mathcal{F}_B$. The distance vector from O_b to an infinitesimal mass element on the right wing, expressed in the right wing reference frame, is calculated using Eq. (27) as $\boldsymbol{C}_{WB}^r\boldsymbol{r}_{wb}^r + \boldsymbol{r}_w^r + \boldsymbol{r}_e^r$. The superscript $(\cdot)^r$ is used to denote the right-wing-related terms. Analogously, the distance vector from O_b to an infinitesimal mass element on the left wing, expressed in the left wing reference frame, is $\boldsymbol{C}_{WB}^l\boldsymbol{r}_{wb}^l + \boldsymbol{r}_w^l + \boldsymbol{r}_e^l$. After defining these distance vectors, the first and second moment of inertia matrices are calculated as

$$\begin{aligned} \tilde{\boldsymbol{S}} &= \int \tilde{\boldsymbol{r}}_f \mathrm{d}m_f + \int \tilde{\boldsymbol{r}}_t \mathrm{d}m_t + \int \tilde{\boldsymbol{r}}_{wb}^r \mathrm{d}m_w^r + \int \tilde{\boldsymbol{r}}_{wb}^l \mathrm{d}m_w^l \\ &\quad + \int (\boldsymbol{C}_{WB}^r)^\intercal(\tilde{\boldsymbol{r}}_w^r + \tilde{\boldsymbol{r}}_e^r)\boldsymbol{C}_{WB}^r \mathrm{d}m_w^r + \int (\boldsymbol{C}_{WB}^l)^\intercal(\tilde{\boldsymbol{r}}_w^l + \tilde{\boldsymbol{r}}_e^l)\boldsymbol{C}_{WB}^l \mathrm{d}m_w^l \\ \boldsymbol{J} &= \int \tilde{\boldsymbol{r}}_f^\intercal\tilde{\boldsymbol{r}}_f \mathrm{d}m_f + \int \tilde{\boldsymbol{r}}_t^\intercal\tilde{\boldsymbol{r}}_t \mathrm{d}m_t + \int \left[\tilde{\boldsymbol{r}}_{wb}^r + (\boldsymbol{C}_{WB}^r)^\intercal(\tilde{\boldsymbol{r}}_w^r + \tilde{\boldsymbol{r}}_e^r)\boldsymbol{C}_{WB}^r\right]^\intercal \\ &\quad \times \left[\tilde{\boldsymbol{r}}_{wb}^r + (\boldsymbol{C}_{WB}^r)^\intercal(\tilde{\boldsymbol{r}}_w^r + \tilde{\boldsymbol{r}}_e^r)\boldsymbol{C}_{WB}^r\right] \mathrm{d}m_w^r \\ &\quad + \int \left[\tilde{\boldsymbol{r}}_{wb}^l + (\boldsymbol{C}_{WB}^l)^\intercal(\tilde{\boldsymbol{r}}_w^l + \tilde{\boldsymbol{r}}_e^l)\boldsymbol{C}_{WB}^l\right]^\intercal \left[\tilde{\boldsymbol{r}}_{wb}^l + (\boldsymbol{C}_{WB}^l)^\intercal(\tilde{\boldsymbol{r}}_w^l + \tilde{\boldsymbol{r}}_e^l)\boldsymbol{C}_{WB}^l\right] \mathrm{d}m_w^l \end{aligned} \tag{B1}$$

The absolute velocity of $\mathrm{d}m_w^r$ has been given in Eq. (A3), in which the term $\boldsymbol{r}_e$ is calculated using Eq. (A1). If the torsional angle θ is assumed to be small, then Eq. (A1) can be linearized as $\boldsymbol{r}_e = [0, 0, w + r_y \cdot \theta]^\intercal$. Because w and θ, respectively, represent the transverse displacement and torsional angle of an arbitrary wing section A_w, then they can be linked to the structural nodal states using shape functions, i.e., $\boldsymbol{r}_e = \Phi(\boldsymbol{r}_w)\boldsymbol{x}_s(t)$. Consequently, $\boldsymbol{v}_e = [\dot{r}_{e,x}, \dot{r}_{e,y}, \dot{r}_{e,z}]^\intercal = \Phi(\boldsymbol{r}_w)\dot{\boldsymbol{x}}_s(t)$. The expressions for $\boldsymbol{r}_e$ and $\boldsymbol{v}_e$ are applicable for both the left and right wings.

Using the generic Lagrangian equations of motion [2,18], the translational dynamic equation of the flexible aircraft expressed in $\mathcal{F}_B$ is

$$m\dot{\boldsymbol{V}}_b = \boldsymbol{F}_{\text{tot}}^B - \tilde{\boldsymbol{S}}^\intercal \dot{\boldsymbol{\omega}}_b - (\boldsymbol{C}_{WB}^r)^\intercal \int \Phi^r \, \mathrm{d}m_w^r \ddot{\boldsymbol{x}}_s^r - (\boldsymbol{C}_{WB}^l)^\intercal \int \Phi^l \, \mathrm{d}m_w^l \ddot{\boldsymbol{x}}_s^l - m\tilde{\boldsymbol{\omega}}_b \boldsymbol{V}_b - \tilde{\boldsymbol{\omega}}_b \tilde{\boldsymbol{S}}^\intercal \boldsymbol{\omega}_b - \tilde{\boldsymbol{\omega}}_b (\boldsymbol{C}_{WB}^r)^\intercal \int \Phi^r \, \mathrm{d}m_w^r \dot{\boldsymbol{x}}_s^r - \tilde{\boldsymbol{\omega}}_b (\boldsymbol{C}_{WB}^l)^\intercal \int \Phi^l \, \mathrm{d}m_w^l \dot{\boldsymbol{x}}_s^l \tag{B2}$$

The translational dynamics expressed in the flight trajectory axes are presented as Eq. (5). Using Eq. (B2), the $\boldsymbol{d}_F$ term in Eq. (5) yields

$$\boldsymbol{d}_F = -(\boldsymbol{C}_{WB}^r)^\intercal \int \Phi^r \, \mathrm{d}m_w^r \ddot{\boldsymbol{x}}_s^r - (\boldsymbol{C}_{WB}^l)^\intercal \int \Phi^l \, \mathrm{d}m_w^l \ddot{\boldsymbol{x}}_s^l - \tilde{\boldsymbol{\omega}}_b (\boldsymbol{C}_{WB}^r)^\intercal \int \Phi^r \, \mathrm{d}m_w^r \dot{\boldsymbol{x}}_s^r - \tilde{\boldsymbol{\omega}}_b (\boldsymbol{C}_{WB}^l)^\intercal \int \Phi^l \, \mathrm{d}m_w^l \dot{\boldsymbol{x}}_s^l \tag{B3}$$

Using the generic Lagrangian equations of motion [2,18], the rotational dynamics expressed in the body frame are presented in Eq. (6), in which

$$\begin{aligned}\boldsymbol{d}_M = &- \int [\tilde{\boldsymbol{r}}_{wb}^r (\boldsymbol{C}_{WB}^r)^\intercal + (\boldsymbol{C}_{WB}^r)^\intercal (\tilde{\mathbf{r}}_w^r + \widetilde{\Phi^r \boldsymbol{x}_s^r})] \Phi^r \, \mathrm{d}m_w^r \ddot{\boldsymbol{x}}_s^r \\ &- \int [\tilde{\boldsymbol{r}}_{wb}^l (\boldsymbol{C}_{WB}^l)^\intercal + (\boldsymbol{C}_{WB}^l)^\intercal (\tilde{\mathbf{r}}_w^l + \widetilde{\Phi^l \boldsymbol{x}_s^l})] \Phi^l \, \mathrm{d}m_w^l \ddot{\boldsymbol{x}}_s^l \\ &- \tilde{\boldsymbol{\omega}}_b \int [\tilde{\boldsymbol{r}}_{wb}^r (\boldsymbol{C}_{WB}^r)^\intercal + (\boldsymbol{C}_{WB}^r)^\intercal (\tilde{\boldsymbol{r}}_w^r + \widetilde{\Phi^r \boldsymbol{x}_s^r})] \Phi^r \, \mathrm{d}m_w^r \dot{\boldsymbol{x}}_s^r \\ &- \tilde{\boldsymbol{\omega}}_b \int [\tilde{\boldsymbol{r}}_{wb}^l (\boldsymbol{C}_{WB}^l)^\intercal + (\boldsymbol{C}_{WB}^l)^\intercal (\tilde{\boldsymbol{r}}_w^l + \widetilde{\Phi^l \boldsymbol{x}_s^l})] \Phi^l \, \mathrm{d}m_w^l \dot{\boldsymbol{x}}_s^l \\ &- \tilde{\boldsymbol{V}}_b (\boldsymbol{C}_{WB}^r)^\intercal \int \Phi^r \, \mathrm{d}m_w^r \dot{\boldsymbol{x}}_s^r - \tilde{\boldsymbol{V}}_b (\boldsymbol{C}_{WB}^l)^\intercal \int \Phi^l \, \mathrm{d}m_w^l \dot{\boldsymbol{x}}_s^l \end{aligned} \tag{B4}$$

References

[1] Avanzini, G., Nicassio, F., and Scarselli, G., "Reduced-Order Short-Period Model of Flexible Aircraft," *Journal of Guidance, Control, and Dynamics*, Vol. 40, No. 8, 2017, pp. 2017–2029. https://doi.org/10.2514/1.G002387

[2] Meirovitch, L., and Tuzcu, I., "Control of Flexible Aircraft Executing Time-Dependent Maneuvers," *Journal of Guidance, Control, and Dynamics*, Vol. 28, No. 6, 2005, pp. 1291–1300. https://doi.org/10.2514/1.12774

[3] Waitman, S., and Marcos, A., "H Infinity Control Design for Active Flutter Suppression of Flexible-Wing Unmanned Aerial Vehicle Demonstrator," *Journal of Guidance, Control, and Dynamics*, Vol. 43, No. 4, 2020, pp. 656–672. https://doi.org/10.2514/1.G004618

[4] Dillsaver, M., Cesnik, C. E., and Kolmanovsky, I., "Trajectory Control of Very Flexible Aircraft with Gust Disturbance," *AIAA Atmospheric Flight Mechanics (AFM) Conference*, AIAA Paper 2013-4745, 2013. https://doi.org/10.2514/6.2013-4745

[5] Drew, M. C., Hashemi, K. E., Cramer, N. B., and Nguyen, N. T., "Multi-Objective Optimal Control of the 6-DoF Aeroservoelastic Common Research Model with Aspect Ratio 13.5 Wing," *AIAA Scitech 2019 Forum*, AIAA Paper 2019-0220, 2019. https://doi.org/10.2514/6.2019-0220

[6] de FV Pereira, M., Kolmanovsky, I., Cesnik, C. E. S., and Vetrano, F., "Model Predictive Control for Maneuver Load Alleviation in Flexible Airliners," *International Forum on Aeroelasticity and Structural Dynamics—IFASD*, Curran Associates, Inc., Red Hook, NY, 2019, pp. 420–432.

[7] Haghighat, S., Liu, H. H. T., and Martins, J. R. R. A., "Model-Predictive Gust Load Alleviation Controller for a Highly Flexible Aircraft," *Journal of Guidance, Control, and Dynamics*, Vol. 35, No. 6, 2012, pp. 1751–1766. https://doi.org/10.2514/1.57013

[8] Nguyen, N. T., Ting, E., Chaparro, D., Drew, M. C., and Swei, S. S.-M., "Multi-Objective Flight Control for Drag Minimization and Load Alleviation of High-Aspect Ratio Flexible Wing Aircraft," *58th AIAA/ASCE/AHS/ASC Structures, Structural Dynamics, and Materials Conference*, AIAA Paper 2017-1589, 2017. https://doi.org/10.2514/6.2017-1589

[9] Hansen, J. H., Duan, M., Kolmanovsky, I., and Cesnik, C. E., "Control Allocation for Maneuver and Gust Load Alleviation of Flexible Aircraft," *AIAA Scitech 2020 Forum*, AIAA Paper 2020-1186.c1, 2020, pp. 1–16. https://doi.org/10.2514/6.2020-1186.c1

[10] Duan, M., Hansen, J. H., Kolmanovsky, I. V., and Cesnik, C. E., "Maneuver Load Alleviation of Flexible Aircraft Through Control Allocation: A Case Study Using X-Hale," *International Forum on Aeroelasticity and Structural Dynamics, IFASD 2019*, Curran Associates, Inc., Red Hook, NY, 2019, pp. 1–16.

[11] Sieberling, S., Chu, Q., and Mulder, J. A., "Robust Flight Control Using Incremental Nonlinear Dynamic Inversion and Angular Acceleration Prediction," *Journal of Guidance, Control, and Dynamics*, Vol. 33, No. 6, 2010, pp. 1732–1742. https://doi.org/10.2514/1.49978

[12] Tipàn, S., Theodoulis, S., Thai, S., and Proff, M., "Nonlinear Dynamic Inversion Flight Control Design for Guided Projectiles," *Journal of Guidance, Control, and Dynamics*, Vol. 43, No. 5, 2020, pp. 975–980. https://doi.org/10.2514/1.G004976

[13] Grondman, F., Looye, G., Kuchar, R. O., Chu, Q., and van Kampen, E., "Design and Flight Testing of Incremental Nonlinear Dynamic Inversion-Based Control Laws for a Passenger Aircraft," *2018 AIAA Guidance, Navigation, and Control Conference*, AIAA Paper 2018-0385, 2018. https://doi.org/10.2514/6.2018-0385

[14] Sun, S., Wang, X., Chu, Q., and de Visser, C., "Incremental Nonlinear Fault-Tolerant Control of a Quadrotor with Complete Loss of Two Opposing Rotors," *IEEE Transactions on Robotics*, Vol. 37, No. 1, 2021, pp. 116–130. https://doi.org/10.1109/TRO.2020.3010626

[15] Mooij, E., "Robust Control of a Conventional Aeroelastic Launch Vehicle," *AIAA Scitech 2020 Forum*, AIAA Paper 2020-1103, 2020. https://doi.org/10.2514/6.2020-1103

[16] Wang, X., van Kampen, E.-J., Chu, Q., and Lu, P., "Stability Analysis for Incremental Nonlinear Dynamic Inversion Control," *Journal of Guidance, Control, and Dynamics*, Vol. 42, No. 5, 2019, pp. 1116–1129. https://doi.org/10.2514/1.G003791

[17] Shearer, C. M., and Cesnik, C. E. S., "Trajectory Control for Very Flexible Aircraft," *Journal of Guidance, Control, and Dynamics*, Vol. 31, No. 2, 2008, pp. 340–357. https://doi.org/10.2514/1.29335

[18] Wang, X., van Kampen, E., Chu, Q. P., and De Breuker, R., "Flexible Aircraft Gust Load Alleviation with Incremental Nonlinear Dynamic Inversion," *Journal of Guidance, Control, and Dynamics*, Vol. 42, No. 7, 2019, pp. 1519–1536. https://doi.org/10.2514/1.G003980

[19] Wang, X., van Kampen, E.-J., Chu, Q., and Lu, P., "Incremental Sliding-Mode Fault-Tolerant Flight Control," *Journal of Guidance, Control, and Dynamics*, Vol. 42, No. 2, 2019, pp. 244–259. https://doi.org/10.2514/1.G003497

[20] Sagliano, M., Mooij, E., and Theil, S., "Adaptive Disturbance-Based High-Order Sliding-Mode Control for Hypersonic-Entry Vehicles," *Journal of Guidance, Control, and Dynamics*, Vol. 40, No. 3, 2017, pp. 521–536. https://doi.org/10.2514/1.G000675

[21] Shtessel, Y., Hall, C., and Jackson, M., "Reusable Launch Vehicle Control in Multiple-Time-Scale Sliding Modes," *Journal of Guidance, Control, and Dynamics*, Vol. 23, No. 6, 2000, pp. 1013–1020. https://doi.org/10.2514/2.4669

[22] Sun, R., Shan, A., Zhang, C., Wu, J., and Jia, Q., "Quantized Fault-Tolerant Control for Attitude Stabilization with Fixed-Time Disturbance Observer," *Journal of Guidance, Control, and Dynamics*, Vol. 44, No. 2, 2021, pp. 449–455. https://doi.org/10.2514/1.G005465

[23] Wang, X., and van Kampen, E., "Incremental Backstepping Sliding Mode Fault-Tolerant Flight Control," *AIAA Scitech 2019 Forum*, AIAA Paper 2019-0110, 2019, pp. 1–23. https://doi.org/10.2514/6.2019-0110

[24] Waszak, M. R., and Schmidt, D. K., "Flight Dynamics of Aeroelastic Vehicles," *Journal of Aircraft*, Vol. 25, No. 6, 1988, pp. 563–571. https://doi.org/10.2514/3.45623

[25] Qi, P., and Zhao, X., "Flight Control for Very Flexible Aircraft Using Model-Free Adaptive Control," *Journal of Guidance, Control, and Dynamics*, Vol. 43, No. 3, 2020, pp. 608–619. https://doi.org/10.2514/1.G004761

[26] Qi, P., Zhao, X., Wang, Y., Palacios, R., and Wynn, A., "Aeroelastic and Trajectory Control of High Altitude Long Endurance Aircraft," *IEEE Transactions on Aerospace and Electronic Systems*, Vol. 54, No. 6, 2018, pp. 2992–3003. https://doi.org/10.1109/TAES.2018.2836598

[27] Edwards, C., and Shtessel, Y. B., "Adaptive Continuous Higher Order Sliding Mode Control," *Automatica*, Vol. 65, March 2016, pp. 183–190. https://doi.org/10.1016/j.automatica.2015.11.038

[28] Lu, P., van Kampen, E.-J., de Visser, C., and Chu, Q., "Aircraft Fault-Tolerant Trajectory Control Using Incremental Nonlinear Dynamic Inversion," *Control Engineering Practice*, Vol. 57, Dec. 2016, pp. 126–141. https://doi.org/10.1016/j.conengprac.2016.09.010

[29] Wang, X., Mkhoyan, T., and De Breuker, R., "Nonlinear Incremental Control for Flexible Aircraft Trajectory Tracking and Load Alleviation," *AIAA Scitech 2021 Forum*, AIAA Paper 2019-0110, 2021, pp. 1–31. https://doi.org/10.2514/6.2021-0503

[30] Chen, Z., "Nussbaum Functions in Adaptive Control with Time-Varying Unknown Control Coefficients," *Automatica*, Vol. 102, April 2019, pp. 72–79. https://doi.org/10.1016/j.automatica.2018.12.035

[31] Lewis, J. A., and Johnson, E. N., "Gain Switching Control Law for Dynamic Inversion Based Adaptive Control with Unknown Sign of Control Effectiveness," *AIAA Scitech 2021 Forum*, AIAA Paper 2019-0110, 2021, pp. 1–25. https://doi.org/10.2514/6.2021-0529

[32] Theodorsen, T., "General Theory of Aerodynamic Instability and the Mechanism of Flutter," NACA TR 496, 1935.